# Can atmospheric chemistry deposition schemes reliably simulate stomatal ozone flux across global land covers and climates?

Tamara Emmerichs[1], Abdulla Al Mamun[2], Lisa Emberson[3], Huiting Mao[4], Leiming Zhang[2], Limei Ran[5], Clara Betancourt[6], Anthony Wong[7], Gerbrand Koren[8], Giacomo Gerosa[9], Min Huang[10], Pierluigi Guaita[9]

[1]Institute of Energy and Climate Systems, Troposphere (ICE-3), Forschungszentrum Jülich, Germany, now at Max-Planck-Institute for Meteorology, Germany

[2]Air Quality Research Division, Science and Technology Branch, Environment and Climate Change Canada, Toronto, Ontario M3H 5T4, Canada

[3]Environment & Geography Department, University of York, York, UK.

[4]Department of Chemistry, State University of New York College of Environmental Science and Forestry, Syracuse, NY, 13210, USA

[5]Soil science and Resource Assessment, National Resource Conservation Service, U. S., Department of Agriculture, Raleigh, NC 27609, USA

[6]AXA Konzern AG, Cologne, Germany

[7]Centre for Global Change Science, Massachusetts Institute of Technology, Cambridge, MA, United States of America

[8]Copernicus Institute of Sustainable Development, Utrecht University, Utrecht, the Netherlands

[9]Dep.t of Mathematics and Physics, Catholic University of the Sacred Heart, Brescia, Italy

[10]Earth System Science Interdisciplinary Center, University of Maryland, College Park, MD, USA

*Correspondence to*: Tamara Emmerichs (tamara.emmerichs@gmx.de)

**Abstract**

28   Over the past few decades, ozone risk assessments for vegetation have evolved two methods based on stomatal
29   $O_3$ flux. However, substantial uncertainties remain in accurately simulating these fluxes. Here, we investigate
30   stomatal $O_3$ fluxes across various land cover types worldwide simulated by six established deposition models.
31   Hourly $O_3$ concentration and meteorological data at nine sites were extracted from the Tropospheric Ozone
32   Assessment Report database, a comprehensive global collection of measurements, for the model simulations.
33   The models estimated reasonable $O_3$ deposition (0.5 - 0.8 cm s$^{-1}$ in summer), which is mostly in agreement with
34   the literature. Simulations of canopy conductance showed differences that varied by land cover type with
35   correlation coefficients of 0.75, 0.80 and 0.85 for forests, crops and grasslands among the models. Differences
36   between models were primarily influenced by soil moisture and vapor pressure deficit, depending on each
37   model's specific structure. Across models, the range of $O_3$ damage simulations at each site was most consistent
38   for crops (6 to 11 mmol $O_3$ m$^{-2}$), followed by forests (3 to 19.5 mmol $O_3$ m$^{-2}$) and grasslands (7 to 33 mmol $O_3$ m$^{-2}$
39   ). The median estimate across models aligns well with the literature at the sites most vulnerable to $O_3$ damage.
40   Overall, this study represents a critical first step in developing and evaluating tools for broad-scale assessment of
41   $O_3$ impacts on vegetation within the framework of TOAR phase II.

43   **1. Introduction**

44   Elevated surface $O_3$ levels significantly damage vegetation due to the stomatal uptake of $O_3$ by canopy leaves.
45   Stomatal uptake of $O_3$ leads to plant tissue injury which in turn causes changes in metabolic functioning,
46   reducing photosynthesis and consequently plant growth and productivity (Mills et al., 2011; Emberson, 2020;
47   Ainsworth et al. 2012; Fuhrer et al., 2016; Grulke and Heath, 2020). Such damage can have significant impacts
48   on crop yields and quality, leading to economic losses and impacting food security in regions already facing
49   scarcity (Avnery et al., 2011; Ainsworth et al. 2017; Ramya et al., 2023). There is an ever-growing body of
50   observational evidence demonstrating a variety of $O_3$ impacts on different ecosystems (crops, forests, grasslands)
51   in North America, Europe and more recently, Asia (Emberson 2020). Various indices assessing $O_3$ exposure to
52   vegetation have been developed over recent decades with the stomatal $O_3$ flux ($POD_y$; phytotoxic ozone dose

53  over a threshold y) index found to provide better estimates of $O_3$ risk to vegetation than the more commonly

54  used concentration-based exposure approaches (e.g., Accumulated Ozone over Threshold (AOT); growing

55  season daylight mean $O_3$ concentration (M7, M12) (Mills et al., 2011; Avnery et al., 2011). A global overview of

56  spatial distribution and trends using concentration-based metrics was provided in the first Tropospheric Ozone

57  Assessment Report (TOAR) by Mills et al. (2018). During TOAR phase II (TOAR-II), here we conduct a flux-

58  based analysis to ensure the most up-to-date vegetation metrics are provided through this community effort.

59  $O_3$ dry deposition to vegetation is in part determined by canopy-level $O_3$ concentrations. A significant fraction of

60  $O_3$ uptake occurs through the plant stomata with the remainder depositing on plant cuticular surfaces and the

61  under-storey vegetation and soil. The stomatal contribution can vary between 50 and 80%, depending on the

62  factors controlling the partitioning of stomatal and non-stomatal uptake (e.g., Huang et al., 2022; Wong et al.,

63  2022; Clifton et al., 2023). As such, quantifying canopy stomatal conductance is important for assessing the

64  mass balance of atmospheric $O_3$ concentrations and its potential damage to vegetation. Both stomatal and non-

65  stomatal processes can vary with environmental conditions such as humidity, solar radiation, temperature and

66  $CO_2$ concentration as well as vegetation type and density (Clifton et al., 2020a). The occurrence of soil water

67  deficit can also play a crucial role where soil water stress induces stomatal closure (Lin et al., 2020; Huang et al.,

68  2022). There are two commonly used stomatal conductance ($g_s$) models - the empirical, multiplicative approach

69  first developed by Jarvis (1976) and the semi-mechanistic coupled net photosynthesis-stomatal conductance

70  models ($A_{net}$-$g_s$). The common Jarvis-type models (e.g. Emberson et al., 2000; Ganzeveld et al., 1995; Zhang et

71  al. 2003), widely applied due to their simplicity and computational efficiency, correct a prescribed maximum

72  stomatal conductance with the multiplication of different environmental factors (e.g., temperature, light, soil

73  water and atmospheric moisture). The $A_{net}$-$g_s$ models couple $g_s$ to plant photosynthesis by calculating the net

74  assimilation of $CO_2$ and estimating gs based on the resulting supply and demand of $CO_2$ (Farquhar et al., 1980;

75  Goudriaan et al., 1985; Ball et al., 1987). $A_{net}$-$g_s$ models involve multiple non-linear dependencies on soil water,

76  humidity and temperature, among other factors defined by measurement constraints (Ball 1987; Leuning et al.,

77  1997). Heterogeneity of stomatal deposition estimates over different land cover types is anticipated, but model

78  uncertainty depends on the representation of the deposition mechanisms, model parameterisation and

79  meteorological inputs (Hardacre et al., 2015; Clifton et al., 2020b; Huang et al., 2022; Khan et al., 2024).

80  Broadly speaking, the pros and cons of these two modelling approaches will tend to depend on the aims of the

81  risk assessment study, the extent of knowledge of the ecosystem being investigated and prevailing bio-climatic

82  conditions. Jarvis-type models are arguably more suitable for studies where less is known about the eco-

83    physiology of the ecosystem since they do not require simulation of net photosynthesis which in itself is

84    inherently difficult to model accurately. However, these models still need to be calibrated for the particular bio-

85    climate of study to ensure temperature and VPD functions are suitable for the prevailing conditions. By contrast,

86    $A_{net}$-$g_s$ models may be more useful for studies where the physiological response to environmental conditions of

87    the ecosystems is reasonably well understood as they can provide insight into not only pollutant deposition, but

88    also how other environmental conditions in addition to pollution may limit plant growth and productivity more

89    generally.

90    In this study, the stand-alone version of six $O_3$ deposition schemes, commonly used in climate or air quality

91    models, are assessed with a focus on their stomatal uptake portion and resulting $POD_y$ calculation. Using

92    concurrent $O_3$ concentration and meteorological variable measurement data from the TOAR database enables us

93    to conduct a detailed intercomparison of multiple deposition schemes by avoiding uncertainties arising from

94    using different input data. For this study, various sites have been selected to represent different land cover types

95    and climate regimes around the globe, focusing on sites where observational data are available for $O_3$

96    concentration. By assessing the model estimates of stomatal $O_3$ deposition at these different sites, we aim to

97    identify key differences in model formulation and parameterisation that influence estimates of stomatal $O_3$ flux

98    and consequent $POD_y$. The estimation of the stomatal uptake from water flux measurements taken from the

99    FLUXNET database provides an additional observational constraint as well as an uncertainty estimate at each

100   site.

101   Furthermore, sensitivity simulations allow us to investigate the variability of stomatal $O_3$ deposition and plant

102   damage with key input parameters and land cover characteristics. Post hoc, plant damage will be calculated

103   offline based on the $POD_y$ simulated by different models and flux-response relationships, where appropriate.

104   Ultimately, we aim to understand the key factors driving stomatal $O_3$ flux and thus $POD_y$ and assess the $O_3$-

105   induced potential for vegetation damage for different land cover types and global regions.

106

107   **2.  Methodology**

108   **2.1 Meteorological and $O_3$ data from the TOAR-II database**

109 The web version of the DO$_3$SE model is coupled to the TOAR database, i.e. the required input data (Table 3) is
110 automatically provided by the database at the respective modelling sites. The TOAR-II database (from now on
111 TOAR) contains harmonised measurements of surface O$_3$ and its important precursors and key meteorological
112 variables that can impact O$_3$ concentrations and stomatal O$_3$ uptake. As one of the largest collections of quality-
113 controlled air pollution measurements in the world, it comprises ground-based station measurements of O$_3$
114 concentration at more than 22905 sites globally which cover different periods between 1974 and 2023. These
115 have been collected from different O$_3$ monitoring networks (e.g., Clean Air Status and Trends Network,
116 CASTNET), harmonised and synthesised to enable uniform processing. The data were selected for inclusion in
117 the TOAR database based on an extended quality control; e.g., sites where the measurement technique changed
118 with time have been excluded. Data errors remain but have been shown to have a minor impact (Schultz et al.,
119 2017). The total uncertainty in modern O$_3$ measurements is estimated to be < 2 nmol mol-1 (Tarasick et al.,
120 2018). The meteorological data (irradiance, air temperature, relative humidity, precipitation, air pressure, and
121 wind speed) in the database stems from the fifth generation of ECMWF reanalysis (ERA5) for global climate
122 (Hersbach et al., 2020). Data re-initialisation (of precipitation and radiation, Copernicus Climate Change
123 Service, 2017) is bridged by (linear) interpolation. The Leaf Area Index (LAI) data in the database stems from
124 the MODerate resolution Imaging Spectroradiometer (MODIS). TOAR data is freely, and openly available
125 through a graphical user interface and a representational State Transfer interface
126 (https://toar-data.fz-juelich.de/api/v2/, last access: 01.11.2024). The TOAR data centre team is committed to the
127 Findability, Accessibility, Interoperability, and Reusability principles (Wilkinson et al., 2016). The centre aims
128 to achieve the highest standards regarding data curation, archival, and re-use (Schröder et al., 2021). To conduct
129 offline simulations with models in addition to Web-DO$_3$SE, the input data were extracted beforehand and proven
130 for identicality. The additionally required data (Table 3) were extracted from the TOAR database and the
131 MeteoCloud server (https://datapub.fz-juelich.de/slcs/meteocloud/index.html) at Forschungszentrum Jülich.

132

133 **2.2 Observation-constrained stomatal conductance**

134 To compare the modelled stomatal conductance with observational information, we prepared model input data at
135 two sites (Hyytiälä, Harvard Forest) from the FLUXNET 2015 dataset (Pastorello et al., 2020), which is openly
136 available under the CC-BY-4.0 data usage licence. Additional vegetation information for the model input (i.e.,
137 LAI, canopy height, and crop calendar data) was provided by the site project investigators. Then, we used the

138    canopy-scale stomatal conductance dataset, SynFlux version 2 to estimate $G_{st}$ for two forest sites, US-Ha1 and

139    FI-Hyy. While in SynFlux version 1, canopy transpiration is assumed to be equal to total latent heat flux

140    SynFlux version 2 improved its previous estimations (Ducker et al., 2018) by using a machine-learning-based

141    method (Nelson et al., 2018) to partition total evapotranspiration into surface evaporation and canopy

142    transpiration. To train quantile random forest models to relate meteorological conditions with water use

143    efficiency (derived from water and carbon fluxes), periods with minimal surface wetness were chosen during the

144    growing season. These models were then used to back-calculate transpiration for the whole growing season.

145    Instead of the total latent heat flux, the resulting transpiration estimate was used as an input to the inverse

146    Penman-Monteith Equation, reducing the potential high bias in the stomatal conductance estimates in SynFlux

147    version 1.

148

149    **2.3 Summary of sites selected for deposition modelling**

150    Nine sites (Table 1) were selected for this modelling work accounting for the following factors: i. geographical

151    spread,including major continents with terrestrial vegetation; ii. land cover/use types, including the plant

152    functional types (PFTs) which are important in terms of economy, food security, or biodiversity and for which

153    we have fairly good knowledge of $O_3$ impacts ; iii. availability of meteorological and $O_3$ data from the TOAR

154    database; iv. availability of observational data describing stomatal conductance of water vapour ($g_{wv}$) estimated

155    from the FLUXNET measurements (Section 2.2); and v. location proximity to previous experiments that have

156    investigated $O_3$ impacts on vegetation that can help interpret our model results.

157    **Table 1. Sites selected for stomatal deposition modelling using data from the TOAR database grouped by**

158    **continent. Sites that also have FLUXNET data are denoted by 'FN' and those with SynFlux data are**

159    **denoted by 'SF'.**

| Site (TOAR station id, nearest FLUXNET site id) | Location, station altitude from TOAR | Köppen-Geiger climate classification | Vegetation details (LAI, canopy height in m) | Record (measurement heights in m) | References |
|---|---|---|---|---|---|
|  |  |  |  |  |  |

| Europe | | | | | |
|---|---|---|---|---|---|
| Hyytiälä, Finland (FI00621, FI-Hyy) FN & SF | 61.8611 °N, 24.2833 °E, 104 m | Dfc | LAI: 2.9 Height: 23.3 | $O_3$: 2014 (4) FLUXNET: 1996/04-2013/09 (14) | Chen et al. (2018); Junninen et al. (2009); Visser et al. (2021) |
| Grignon, France (FR04038, FR-Gri) FN | 48.5819 °N, 1.833 °E, 165 m | Cfb | LAI: 4.3 Height: 3.5 | $O_3$: 2013/2014 (3) FLUXNET: 2004-2014 (2) | Stella et al. (2013) |
| Castelporziano, Italy (IT0952A, IT-Cpz) | 41.8894 °N, 12.266 °E, 19 m | Csa | LAI: 6.9 Height: 14.0 | $O_3$: 2013/2014 (19.7) FLUXNET: 2013/2014 (10) | Gerosa et al. (2005, 2009); Fares et al. (2009, 2012); personal communications with Silvano Fares |
| Asia | | | | | |
| Amberd, Armenia (AM0001R) | 40.3844 °N, 44.2605 °E, 2080 m | BSk (or Dfa) | LAI: 3.9 Height: 1.0 | $O_3$: 2009/2010 (3) | |
| Pha Din, Vietnam (VN0001R) | 21.5731 °N, 103.5157 °E, 1466.0 m | Cwa | LAI: 6.9 Height: > 10.0 | $O_3$: 2015-2017 (12) | Pieber et al. (2023); Bukowiecki et al. (2018); Yen et al. (2013) |
| North America | | | | | |
| Quabbin Reservoir/Har | 42.2985 °N, -72.3341 °E, | Dfb | LAI: 3.0 Height: 24.0 | $O_3$: 2010-2012 (2) | Clifton et al. (2019, 2020b); |

| | | | | | |
|---|---|---|---|---|---|
| vard Forest tower, USA (25-015-4002, US-Ha1) FN & SF | 312 m | | | FLUXNET: 1993-2012 (24) | Ducker et al. (2018) |
| Nebraska, USA (31-055-0032, US-Ne3) | 41.3602 °N, -96.0250 °E, 400 m | Dfa | LAI: 1.7 Height: 2.5 | O$_3$: 2010 (2) FLUXNET: 2013/04- (0.5) | Amos et al. (2005); Leung et al (2020) |
| South America | | | | | |
| Huancayo, Peru (PE0001R) | -12.0402 °N, -75.3209 °E, 3314 m | Cwb | LAI: 3.6 Height: 1.0 | O$_3$: 2015 (6) | |
| Africa | | | | | |
| Mt. Kenya, Kenya (KE0001G) | -0.062 °N, 37.297 °E, 3678.0 m | Aw | LAI: 4.2 Height: 1.0 | O$_3$: 2015 (unknown) | Henne et al. (2008a,b) |

160

161 **Table 2. Land cover type, species and growing season (where SGS = start of growing season and EGS =**
162 **end of growing season) by site. The equivalent land cover type and soil texture data used by the models**
163 **used in this study (Section 2.3) are also shown. MESSy does not consider different land cover types.**
164 **Models that do not consider soil type (i.e. do not include an estimate of soil moisture influence on stomatal**
165 **deposition) are marked with \*.**

| Station site: land cover type (species) and | Web-DO$_3$SE | TEMIR* | NOAH-GEM | ZHANG* | CMAQ |
|---|---|---|---|---|---|

| growing season | | | | | |
|---|---|---|---|---|---|
| Hyytiälä, Finland: evergreen needleleaf forest (Scots pine) SGS=1, EGS=366 | evergreen needleleaf forest, loam | evergreen needleleaf boreal forest | evergreen needleleaf forest, organic material | evergreen needleleaf forest | evergreen needleleaf forest, silty loam (peat) |
| Grignon, France: crops (rapeseed and wheat) SGS=304, EGS=571 | winter wheat, loam | C3 crop | crops/ grassland mosaic, silt loam | crops | crops (wheat), silty loam |
| Castelporziano, Italy: evergreen broadleaf forest (laurel, abutus, broad-leaved phillyrea, holm oak, pine) SGS=1, EGS=366 | evergreen broadleaf forest, loam | Evergreen broadleaf temperate forest | evergreen broadleaf forest, sandy loam | evergreen broadleaf forest | evergreen broadleaf forest, loamy sand |
| Amberd, Armenia: Grassland, mixed SGS=1, EGS=366 | grassland, loam | grassland | grassland, loam | long grassland | grassland, loam |
| Pha Din, Vietnam: evergreen needleleaf forest SGS=1, EGS=366 | evergreen needleleaf forest, loam | evergreen needleleaf temperate forest | evergreen needleleaf forest, clay | evergreen needleleaf forest | evergreen needleleaf forest, clay |
| Quabbin Reservoir/Harvard Forest tower, USA SGS=93, EGS=312 | temperate mixed forest, loam | deciduous broadleaf temperate forest | deciduous broadleaf forest, sandy loam | deciduous broadleaf forest | deciduous broadleaf forest, sandy loam |
| Nebraska, USA: crops (maize/soybean rotation) SGS=132/148, | crops (maize, soybean), loam | C3 crop | crops/ grassland mosaic, silty | crops | crops (corn), silty clay loam |

| | | | clay loam | | |
|---|---|---|---|---|---|
| EGS=278/260 | | | clay loam | | |
| Huancayo, Peru: grassland SGS=1, EGS=366 | grassland, loam | grassland | grassland, loam | long grassland | grassland, loam |
| Mt. Kenya, Kenya: grassland, shrublands SGS=1, EGS=366 | grassland, loam | grassland | grassland, loam | long grassland | grassland, silty loam |

166

167
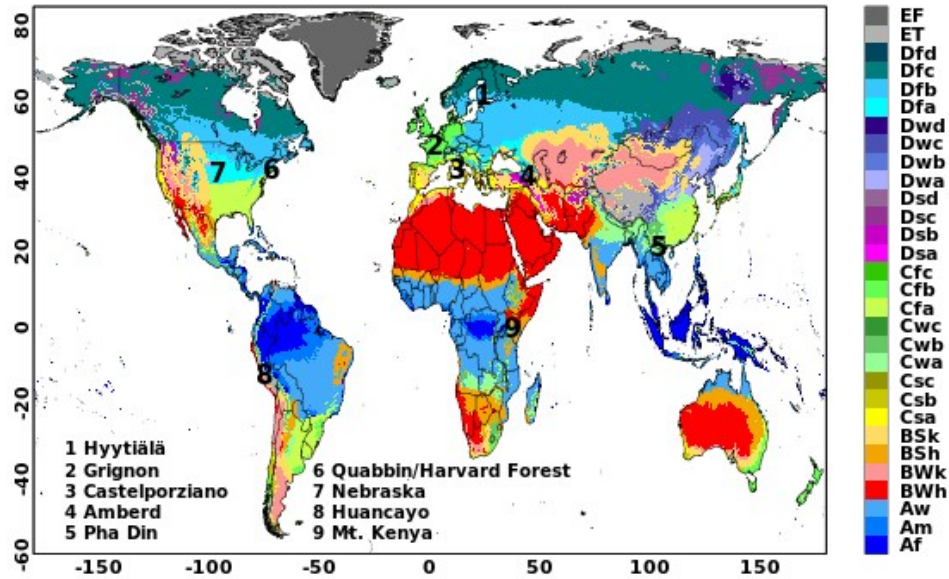
**Fig. 1: Locations of 9 selected sites on Köppen-Geiger climate classification map for 1991-2020 (source: Beck et al., 2023). Table 1 specifies the classifications of these sites.**

**2.3 Stomatal deposition models and their key inputs**

Six widely used empirical/Jarvis and semi-empirical/Ball-Berry types of stomatal deposition models were selected for this study. All of these used models can accommodate a variety of land cover/land use types and

168
169
170
171
172

173    provide estimates of stomatal deposition that can be output as both hourly- and season-long cumulative-stomatal

174    deposition metrics. The key model features are described below.

175    (1)  The empirical/Jarvis-type models use a predefined stomatal conductance modified with different

176         environmental stressors for radiation (PAR), air temperature (T), vapour pressure deficit (VPD) and soil

177         water (SM) - The ZHANG model (Zhang et al., 2002; 2003; 2006) and the Web-DO$_3$SE model (i.e., a

178         version of DO$_3$SE that is directly coupled to the TOAR database, Emberson et al. 2000) account for

179         sunny and shaded leaves (two-big leaf), the Web-DO$_3$SE model also depends on the vegetation

180         phenology, the CMAQ_J model (Pleim and Ran, 2011) and the MESSy model (Ganzeveld et al., 1995;

181         Kerkweg et al., 2006) account for one-big leaf CMAQ_J uses relative humidity (RH) instead of VPD.

182         MESSy calculates the initial stomatal conductance based on the PAR and several empirical parameters

183    (2)  Semi-empirical/Ball-Berry - The CMAQ_P model  (Ran et al,. 2017) and the TEMIR model (Collatz et

184         al., 1991; Farquhar et al., 1980) calculate the stomatal conductance at sunlit and shaded leaves for C3

185         and C4 plants depending on net $CO_2$ assimilation rate, $CO_2$ partial pressure, atmospheric pressure (Pa)

186         and water vapor pressure for each leave. The  NOAH-GEM model is different, calculating stomatal

187         conductance at one big leaf using RH instead of VPD  (Wu et al., 2011; Niyogi et al., 2009).

188    All models follow the resistance scheme:

189
190
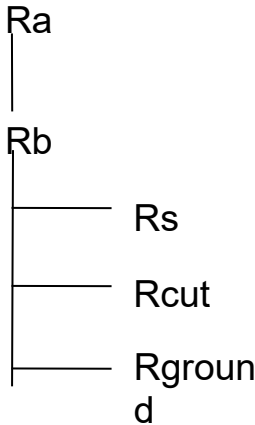
191 The land cover, growing season, and soil texture specifications used by the models are summarised in Table 2.

192 For crops, we used the GGCMI Phase 3 crop calendar (Jägermeyr et al., 2021a) which provides the planting date

193 and maturity day for 18 different crops at a 0.5° land grid cell resolution (Jägermeyr et al., 2021b). For forest

194 trees, we consider four various classes: evergreen-needleleaf (EN), evergreen-broadleaf (EB), deciduous

195 needleleaf (DN), and deciduous broadleaf (DB). For evergreen species, we assume a year-round growing season;

196 for deciduous species, we use the simple latitude function described in Hayes et al.(2017); and we consider a

197 year-round growing season for tropical species. The soil texture categories used by the models were obtained

198 from the reference studies in Table 1 and the site principal investigators. Table 3 provides the key formulas,

199 input data requirements and references for all models. Key total and stomatal deposition parameters for

200 empirical models ($g_{max}$) and semi-empirical models ($V_{Cmax}$) are described in Table 4, which gives a good

201 indication of the overall difference in the magnitude of stomatal deposition. The models' meteorological and $O_3$

202 inputs have been introduced in Section. 2.1.

203

204 **Table 3. Stomatal deposition models selected for site-scale modelling (list of symbols: A1 and Section S3 in**

205 **the SI, \*uses u(h), o3(h)=1, for US-Ne: u(h), o3(h)=0.3).**

| Model | Approach | Key Formulas | Key Input data | Reference |
|---|---|---|---|---|
| ZHANG | Empirical (Jarvis-style) | $$R_s = \cfrac{1}{\left[ Gs(PAR)f(T)f(D)f(\psi) \times \cfrac{D_i}{D_v} \right]}$$  $$G_s(PAR) = \cfrac{L_{sun}}{r_s(PAR_{sun})} + \cfrac{L_{shade}}{r_s(PAR_{shade})}$$ | LAI, LUC, Wspeed, ssrd, T2m, Tskin, RH | Zhang et al., 2002; 2003; 2006 |

| | | | | |
|---|---|---|---|---|
| | | $$r_s(PAR)=r_{s,min}\left(1+\dfrac{b_{rs}}{PAR}\right)$$ | | |
| Noah-GEM | Semi-empirical, photosynthesis-based (Ball-Berry type) | $$R_s=1/\left[LAI\left(\dfrac{m\,A_n\,h_s\,P}{C_s}+b\right)\right]$$ | LAI, LUC, Wspeed, ssrd, strd, T2m, Tskin, RH | Wu et al., 2011; Niyogi et al., 2009 |
| CMAQ_J | Empirical (Jarvis-style) | $$R_s=\dfrac{r_{s,min}\,LAI}{\left(f_{PAR}\,f_T\,f_{vpd}\,f_w\right)}$$ | LAI, Tair, PAR, ssrd, rn, RH SM | Pleim & Ran 2011 |
| CMAQ_P | Semi-empirical, photosynthesis-based (Ball-Berry type) | $$R_s=1/\left(\dfrac{m_g\,A_{net}\,e_s\,P_a}{C_s}\,e_i+g_0\right)$$ | LAI, $CO_2$, Pa, u*, h_dis, z0, SM, Tsoil, wspeed, wdir, Soil texture, C3/C4 type, PAR, | Ran et al,. 2017 |

| | | | ssrd, rn, P_rate, sn, sd | |
|---|---|---|---|---|
| **TEMIR** | Semi-empirical, photosynthesis-based (Ball-Berry type) | $$R_s = \cfrac{1}{\left[\left(\cfrac{L_{sun}}{r_b+r_{sun}}+\cfrac{L_{shade}}{r_b+r_{shade}}\right)\cfrac{D_i}{D_v}\right]}$$  $$r_s = \cfrac{1}{g_s} = \cfrac{1}{\left[\alpha\left(\cfrac{m\,A_n\left(\cfrac{e_s}{e_{sat}}\right)}{\left(\cfrac{C_s}{P_{atm}}\right)}+b\right)\right]}$$ | LAI, LUC, u*, ssrd, T2m, Tskin, RH, SM | Tai et al., 2024; Sun et al., 2022 |
| MESSy | Empirical (Jarvis-style) | $$R_s = \left[r_s(PAR,LAI)\right]f_T\,f_{vpd}\,f_w\right] \times \frac{D_v}{D_i}$$  $$r_s(PAR,LAI) = kc\,x$$ $$\left[\frac{b}{d\,PAR}\ln\left(\frac{\exp(kLAI)+1}{d+1}\right) - \ln\left(\frac{\exp(-kLAI}{d+1}\right)\right.$$ | LAI, ssrd, RH, sw, Tir | Emmerichs et al., 2021; Kerkweg et al., 2006; Ganzeveld et al., 1998 |
| Web-DO$_3$SE | Empirical (Jarvis-style) | $$r_s = g_{max}\,max\left\{\left(f_{min},f_{temp},f_{VPD},f_{SWC}\right)\right\} \times f_{phen} \times f_{light}$$ | Tair, VPD  wspeed, P, Pa, O$_3$, Gr | Emberson et al., 2000; Bueker et al., 2012; Simpson et al., 2011; Guaita et al., 2023a |

206

207

**Table 4 Model parameter $V_{Cmax}$ at standardised temperature conditions (25°C) [in μmol $CO_2$ m$^{-2}$ s$^{-1}$ ] and $g_{max}$ [$O_3$ in cm s$^{-1}$ ] for the total canopy by land cover/land use type. Note that the values presented in the table were recalculated from the original respective rsmin values for $H_2O$ (s m$^{-1}$) in ZHANG, MESSy, and CMAQ_J, and $Vc_{max}$ values for $O_3$ (mol $O_3$ m$^{-2}$s$^{-1}$) in Web-DO$_3$ SE .**

| Parameter | Web-DO$_3$SE | ZHANG | CMAQ_J | TEMIR | NOAH-GEM | CMAQ_P |
|---|---|---|---|---|---|---|
| $G_{max}$ or $V_{Cmax}$ | $g_{max}$ [cm s$^{-1}$] | $g_{max}$ [cm s$^{-1}$] | $g_{max}$ [cm s$^{-1}$] | $V_{Cmax}^{+}$ [μmol $CO_2$ m$^{-2}$ s$^{-1}$] | $V_{Cmax}$ [μmol $CO_2$ m$^{-2}$ s$^{-1}$] | $V_{Cmax}$ [μmol $CO_2$ m$^{-2}$ s$^{-1}$] |
| Forests | 0.44 (EN) 0.49 (EB) 0.55 (DB) | 0.25 (EN) 0.42 (EB) 0.42 (DB)<br><br>Zhang et al., 2003 | 0.36 (EN), 0.53 (EB), 0.32 (DB),<br><br>Pleim & Ran, 2011 | 60.1 (EN) 59.0 (EB) 55.4 (DB),<br><br>(Oleson et al, 2013; NCAR Technical notes) | 57.6 (EN) 96 (EB) 96 (DB)<br><br>Niyogi et al., 2009; JAMC | 57.6 (EN, Slevin et al 2015), 49.2 (EB, Medi. forest, (EB_tr+EB_te)/2,Oliver et al., 2022), 55.4 (DB, CLM4.5, Kattge 2009) |
| Crops | 1.1 (wheat) 0.74 (maize) 0.73 (soybean) | 0.53 | 0.91 | 96.7 | 76.8 | 96.7 (CLM4.5) |

| | | | | | | |
|---|---|---|---|---|---|---|
| Grasses | 0.66 | 0.64 | 0.64 | 75.1 | 28.8 | 75.1 (CLM4.5) |

212

213  POD$_y$ is calculated in post-processing, according to the guidelines in UNECE LRTAP (2017):.

214  $$POD_y = \sum_{i=1}^{n} \left[ fst, sun_i - y \right] \times \left( \frac{3600}{10^6} \right) \quad \text{for } fst, sun_i \geq y \, nmol \, m^{-2} PLA \, S^{-1}$$

215  Where $fst, sun_i$ is the hourly mean $O_3$ flux in nmol $O_3$ m$^{-2}$ PLA s$^{-1}$ at sunlit leaves, $y$ is a species-dependent

216  threshold (crops: 6 nmol $O_3$ m² s$^{-1}$, grassland and forests:1 nmol $O_3$ m$^{-2}$ s$^{-1}$; UNECE LRTAP (2017) and i is the

217  number of daylight hours (when ssrd > 50 W m$^{-2}$) within the accumulation period (growing season). The term

218  (3600/10$^6$) converts from nmol m$^{-2}$ PLA s$^{-1}$ to mmol $O_3$ m$^{-2}$ PLA. $fst, sun$ is calculated by:

219  $$f_{st,sun} = c \frac{(z) \times g_{st} \times r_c}{r_b + r_c}$$

220  Where c(z) is the $O_3$ concentration at in nmol m$^{-3}$ (calculated from ppb by multiplying by P/RT where P is the

221  atmospheric pressure (Pa) and T is the air temperature (K), R is the universal gas constant of 8.31447 J mol$^{-1}$ K$^{-1}$

222  and T is the assumed standard air temperature (293 K). The leaf surface resistance (r$_c$) is given by r$_c$ = 1/(g$_{st}$+g$_{ext}$)

223  where g$_{ext}$ is the inverse of cuticular resistance.

224  . The leaf boundary resistance is calculated by:

225  $$r_b = 1.3 \times 150 \times \sqrt{\frac{L}{u(h)}}$$

226  Where factor 1.3 accounts for the differences in diffusivity between heat and $O_3$, $L$ is the crosswind leaf

227  dimension (i.e. leaf width in m) and $u(h)$ is the wind speed at the top of the canopy.

228  **2.4 Description of stomatal deposition model simulations**

229 The result section aims at identifying trends in stomatal deposition models among different land cover types
230 including grass, crops and forests using four model experiments as follows.

231 **In experiment 1**, the different models are driven by the $O_3$ and meteorological data from ERA5. We analysed
232 the simulated deposition velocity ($V_d$) split into stomatal and non-stomatal fractions, canopy ($G_{st}$) and sunlit
233 ($G_{sun}$) stomatal conductance.

234 To include observational constraints, in **experiment 2,** the TEMIR, ZHANG, NOAH, MESSy and CMAQ
235 models were run with data obtained from the FLUXNET database (available for three sites, see Table 1), and the
236 simulated $G_{st}$ was evaluated with observation-derived values, inferred $G_{st}$, of SynFlux. Spearman correlation was
237 applied for the model evaluation, as it can be applied to any datasets including non-parametric and non-linear
238 ones. The US-Ha1 and FI-Hyy sites were considered for the model evaluation due to the availability of SynFlux
239 data at these sites

240 A sensitivity analysis (**experiment 3**) was performed by driving a set of models with synthetic input data in the
241 following steps: i. $O_3$ input was perturbed by +/- 40% (Sofen et al. 2016). ii. soil water content was perturbed by
242 +/- 30 % (Li et al., 2020). iii. absolute humidity was perturbed by +/- 30%, soil and air temperatures were
243 perturbed by +/-3, independently, iv. the growing season, which was mostly approximated by LAI, was shifted
244 by 14 days forward and backward in time. In set (iii) and (iv), relative humidity was calculated from absolute
245 humidity and temperature after their perturbation. In both cases, absolute humidity was capped at the saturation
246 vapour pressure at the corresponding temperature.

247 Finally, for **experiment 4,** $g_{max}$ and $V_{Cmax}$ of the models were varied by +-20 %, based on previous estimates of
248 plant traits dependent uncertainty (e.g., Walker et al., 2017; UNECE LRTAP, 2017).

249 **3. Results**

250 **3.1 General characteristics of simulated total deposition velocity and stomatal contribution**

251 The split of total $O_3$ deposition between different pathways, $G_{st}$, $G_{cut}$, $G_{ground}$, simulated by the 7 models is shown
252 for each of the 9 sites in Figure 2 and S2 (corresponding data are presented in Table S9). This analysis allows us
253 to briefly assess the overall efficacy of the model's ability to simulate deposition velocity $V_d$ (by comparisons
254 with previously published values; more complete assessments of model's ability for some of these sites can be

255    found in Clifton et al., 2023) and to compare the importance of the stomatal deposition pathway between models

256    for different land cover types and across different seasons.

257    Observations of $V_d$ have only been made at a handful of sites i.e. Hyytiälä, Finland; Castelporziano, Italy;

258    Grignion, France and Harvard Forest, US (close to our Quabbin site in terms of proximity, land cover type and

259    climate). Overall, the models capture $V_d$ at these sites compared to observed values reported in previous studies.

260    Namely, the observed seasonal cycle in $V_d$ at Hyytiälä, Finland (needleleaf forest), with lows of ~0.1 cm s$^{-1}$

261    between January and April and highs of 0.4 cm s$^{-1}$ between June to September, averaged over 10 years of

262    measurements from Clifton et al. (2023) and Visser et al. (2021) are captured by most models except of MESSy

263    and TEMIR, which reach $V_d$ values of 0.8 cm s$^{-1}$ during the summer. Similarly, the strong seasonal cycle in $V_d$ at

264    Quabbin, US (temperate mixed forest), ranging from around 0.2 cm s$^{-1}$ between January and April up to 0.5 cm

265    s$^{-1}$ from June to September in Clifton et al. (2023) is captured by all models. Observed $V_d$ at Castelporziano,

266    Italy (evergreen broadleaf forest) shows relatively constant values throughout the year, commonly between 0.4

267    and 0.8 cm s$^{-1}$ averaged over a 2-year period (Savi & Fares, 2014). The study by Stella et al. (2011) reports $V_d$

268    measurements of 0.63 cm s$^{-1}$ (on average) at Grignion (France). At the other sites, no $O_3$ dry deposition

269    measurement exists and thus we report the observed ranges for the land cover type (and possibly the matching

270    climate). Over grassland, Silva and Heald (2018, and references therein) show a mean of 11 measurements of

271    daytime $V_d$ values (~0.4 cm s$^{-1}$) in agreement with our models. Measurements exist at soybeans and maize crops

272    which indicate $V_d$ values of 0.7 (Meyers et al., 1995) and 0.4 - 0.6 cm s$^{-1}$ (Stella et al., 2011), respectively. Thus,

273    the models seem to estimate too low deposition at soybeans.

274    In terms of deposition pathways, for all sites and models, stomatal deposition consistently ranks as the most

275    important pathway in the summer, whereas in winter and, for some models, in the fall $G_{st}$ decreases to zero to

276    very low at sites with seasonal variation in vegetation coverage. The importance of the pathway varies with land

277    cover type and season. The highest stomatal contribution of 90 % (NOAH model) is shown at the Amberd site.

278    Among the different land cover types, the highest average stomatal contribution to deposition during the summer

279    is estimated across grass (67 %), followed by crops (65 %) and forests (59 %). The seasonal importance of

280    stomatal contribution is not seen for the tropical sites as the year- round growing season means that stomatal

281    conductance is driven by solar radiation which is constant throughout the year (e.g. Hardacre et al., 2015).

282    Previous studies involving measurements and partitioning approaches (Horvath et al., 2018, Meszaros et al.,

283    2009) indicate that the non-stomatal $O_3$ deposition pathways (i.e., $G_{ground}$ and $G_{cut}$) are very strong (in some cases,

284    dominant over $G_{st}$) at short vegetation such as the grasslands. Despite there are multiple factors such as wind

285    speed, solar radiation, LAI, etc., that control the relative contributions of the three deposition branches, $G_{st}$ is the

286    dominant pathway at the three grassland sites of the current study (Amberd, Mt Kenya, and Peru). At the

287    Amberd and Peru sites, $G_{cut}$ and $G_{ground}$ are small since low wind speed reduces downward mixing of ozone to the

288    surface (atmospheric resistance, e.g., at the Peru Site in the Summer season, the mean wind speed was 1.0 cm s$^{-1}$

289    and the $G_{cu}$ and $G_{ground}$ contributions in the TEMIR model were 21 % and 12 %, respectively; Table S3).

290    In contrast, at the Mt Kenya site, $G_{st}$ exceeds $G_{cut}$ and $G_{ground}$, since the strong solar radiation (annual mean is 246

291    W m$^{-2}$, Table S2) at this site favours stomatal opening . Besides that, LAI is a very important governing factor

292    for $G_{st}$ . Therefore, it can be inferred that the $O_3$ deposition pathway depends on not only the land cover type but

293    also meteorological drivers. The relative contributions of each deposition pathway depends on the interplay

294    between these key factors at a particular site. Among the models, Web-DO$_3$SE estimated the lowest stomatal

295    contribution at grass (Fig. 2) most likely due to its parallel pathways to cuticle, soil and stomata, with the former

296    scaled by LAI with a constant cuticular deposition of 2500 s m$^{-1}$. Such differences in model structures likely led

297    to the wide-ranging partitioning. For example, for the Quabbin site (summer), all models simulate $G_{cut}$ ranging

298    from 15-65 %, $G_{ground}$ from 2-19 % and $G_{st}$ from 33-66 % despite their agreement on  the overall $V_d$ values (total

299    bar). Models agree better in the partitioning of $O_3$ dry deposition to crops with summer stomatal fraction

300    contributions ranging between 46-73 %, 37-73 % and 51-81 % for US-Ne3 Maize, US-Ne3 soybeans and FR-

301    Gri (rapeseed and wheat). Most models estimate non-stomatal deposition equal to or larger than the stomatal

302    contribution to deposition outside of the tropics in winter and fall, and to some extent in spring. This again

303    emphasises the importance of the stomatal contribution to the seasonal cycle of total deposition as also found in

304    Clifton et al. (2023). Similarly, as seen at grasslands, Web-DO$_3$SE (Fig. 2, Table S3) accounts for the highest

305    non-stomatal deposition at crop sites.

306    Across all forest sites, models show significant cuticular uptake throughout the year ranging between 11 % and

307    94 % contribution. At FI-Hyy, $G_{cut}$ averages ~50 % across all seasons and all models with higher estimates of

308    ~55 % by the TEMIR model due to the higher wind speed at FI-Hyy (annual mean wind speed is 3.2  m s$^{-1}$; Table

309    S2) favoring cuticular deposition as suggested by Rannik et al. (2012). At IT-Cpz, our models estimate on

310    average around 43 % (20-80 %) to be non-stomatal deposition, close to the previously reported ranges (Gerosa et

311    al. 2005, Fares et al. 2012, Fares et al. 2014), which were up to 57 % from non-stomatal deposition and 30-60 %

312    from stomatal uptake. A similar partitioning (59 % $G_{st}$, 33 % $G_{cut}$, 5 % $G_{ground}$ model average in summer) is seen

313    at PhaDin.

314

315
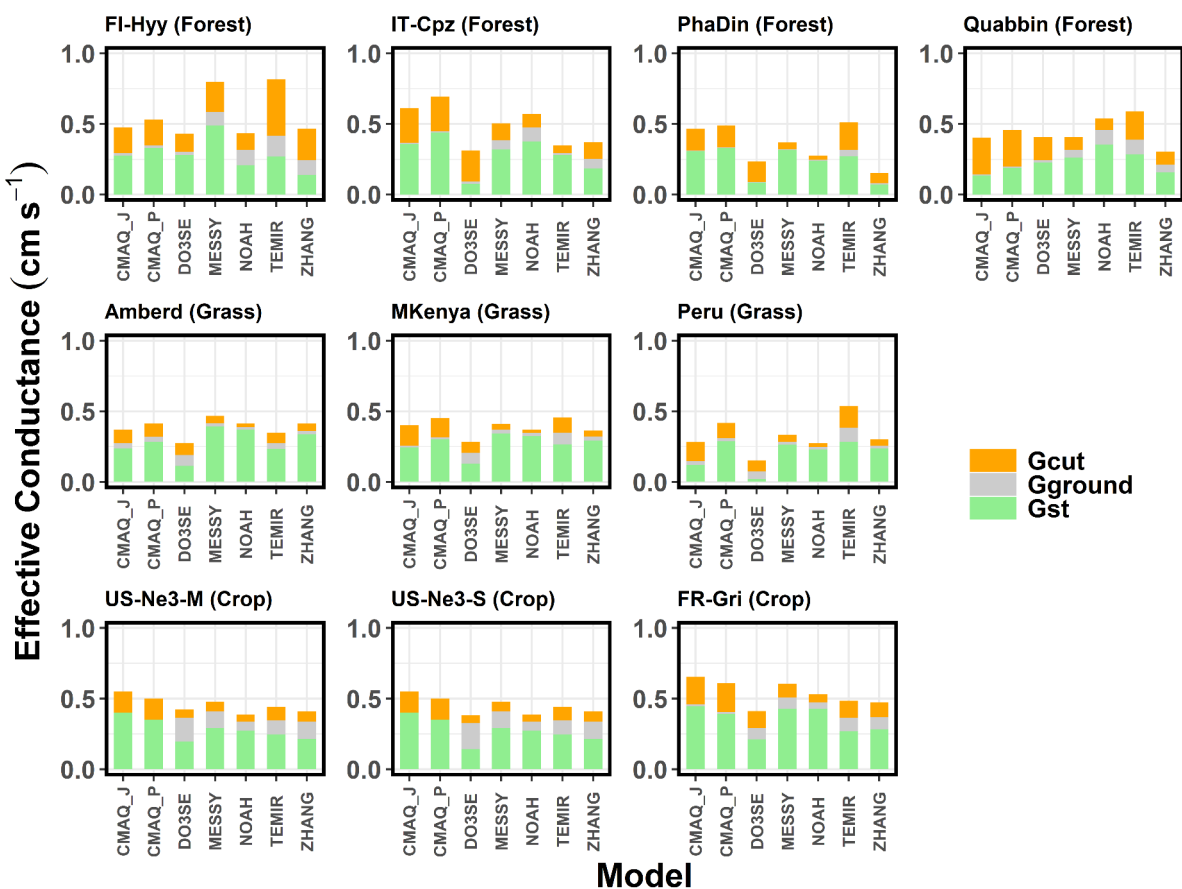
**Fig. 2** Mean effective conductanceof the cuticular ($G_{cut}$), ground ($G_{ground}$), and stomatal ($G_{st}$) deposition pathways of $O_3$ across various models and sites during the summer season (US-Ne3-S=soybeans, US-Ne3-M=maize). Respective figures for the other seasons are presented in the supplement.

319

All models except Web-DO$_3$SE were compared on a seasonal and hourly basis with the SynFlux $G_{st}$ data for US-Ha1 and FI-Hyy sites (Figures S2, S3). CMAQ_J, NOAH, TEMIR, and ZHANG show reasonable agreement at the Quabbin forest (US-Ha1) whereas CMAQ_P and MESSy show quite significant overestimates at both FI-Hyy and Harvard Forest (Table S5) and CMAQ_J overestimates at FI-Hyy only. Note that NOAH and ZHANG show significant underestimates at FI-Hyy while agreeing well with SynFlux at Harvard Forest (Quabbin). The

325    underestimates by the ZHANG model are consistent with the results from a similar comparison for Yellowstone

326    National Park in the US by Mao et al. (2024). Compared to Harvard Forest, FI-Hyy is the most humid and

327    cloudy with the lowest solar radiation flux, and these conditions likely contribute to the underestimates by the

328    NOAH and the ZHANG model as identified by Mao et al. (2024). The differences between modelled and

329    SynFlux $G_{st}$ do not seem to be associated with the model types, i.e. empirical or photosynthesis-based models.

330    The correlation of the diurnal cycle of $G_{st}$ calculated by the models with the inferred $G_{st}$ by SynFlux for US-Ha1

331    and FI-Hyy (Fig. S4) confirms that models generally capture the temporal patterns of $G_{st}$ of at least these two

332    different forest types and climates (FI-Hyy: EN, temperate, subarctic; Quabbin: DB, moist temperate). The best

333    Spearman correlations are found at FI-Hyy and range between 0.73 by the MESSy model and 0.85 by the

334    TEMIR model. Overall lower correlations are found at the Quabbin site ranging from 0.65 for the NOAH and

335    MESSy models to 0.82 for the CMAQ_P model. This poorer correlation suggests that additional water stress

336    may limit stomatal conductance at Quabbin, which the models do not capture, compared to FI-Hyy. Notably, a

337    similar range of correlation coefficients (0.61 – 0.93) was found when modelled $G_{st}$ values obtained using the

338    TOAR input data were compared with SynFlux $G_{st}$. As SynFlux data were generated using FLUXNET

339    measurement data, this result corroborates the validity of using the TOAR database as input to Web-DO$_3$SE,

340    developed as a service website to aid in risk assessment of $O_3$ damage to European vegetation.

341    To identify the key drivers of the $G_{st}$ model schemes among different land cover types and climate conditions,

342    we also compare estimates of $G_{st}$ between models for all sites and analyse the similarity of $G_{st}$ diurnal cycles in

343    empirical and photosynthesis models. Here, it is important to understand the model distinction between shaded

344    and sunlit leaf ($G_{sun}$, Fig 4). The average diurnal variations of stomatal conductance ($G_{st}$) of $O_3$ at the 9 sites for

345    each season are shown in Figure 3 and S7. This also helps interpret the modelled stomatal conductance of sunlit

346    leaves ($G_{sun}$) shown in Fig 4 and S8. Across all models, the diurnal mean $G_{st}$ (Fig. 3) varied from 0.15 cm s$^{-1}$

347    (Quabbin) to 0.50 cm s$^{-1}$ (Mt. Kenya). In the TEMIR and the ZHANG model, roughly 50% of $G_{st}$ occurs at the

348    sunlit part of the leaves. Web-DO3SE and CMAQ_P $G_{sun}$ contribute 30 % on average (Fig. 4). At mid-to-high

349    latitudes, the model spread is limited to the summer season, whereas at tropical sites, it is similar throughout the

350    year. During the day, models show a spread of 1.2 cm s$^{-1}$ in $G_{st}$ at the forest and grassland sites during the

351    summer while their predictions agree most at the crop sites (throughout the year) with a maximum of 1.0 cm s$^{-1}$.

352    This is due to the flux response relationship which has a more sensitive response (steeper slope for most crops)

353    due to a higher threshold (see Table 5 for the equations describing the steepness of the change). Results among

354    the same model type differed significantly while different model types could produce similar results at the same

355    location. For the sites with distinct seasonal variations, model differences were the largest in summer.

356    In comparison, TEMIR and ZHANG, photosynthesis-based and Jarvis-style, respectively, are both governed

357    mainly by solar radiation (see higher $G_{sun}$ in Fig. 4), showing close agreement, except in summer, at the forest

358    sites (ZHANG values are very low). Only these two show a midday depression in $G_{sun}$ at the peak of solar

359    radiation at Mt Kenya (the site with the highest radiation). The ZHANG model also estimated this feature for

360    $G_{sun}$ and $G_{st}$ at other grassland sites (Fig. 3 and 4). This feature could be due to the day length (seasonality)

361    scaling of $V_{Cmax}$ in TEMIR, causing $G_{st}$ to increase significantly during summer at higher latitude sites. In

362    contrast, at lower latitude sites (Mt Kenya and Huancayo, Peru), the seasonal variation in day length is smaller

363    and subsequently smaller seasonality in $V_{Cmax}$ and $G_{st}$. The TEMIR and the CMAQ_P models, both

364    photosynthesis-based, estimate very similar $G_{sun}$ values (Fig. 4) at PhaDin (fall, winter), IT-Cpz (spring,

365    summer) and FI-Hyy (summer) whereas the $G_{st}$ estimates show significant differences. The opposite occurs at

366    Quabbin where the $G_{sun}$ values of the two models differ much more than the $G_{st}$ estimates. These results illustrate

367    that the different fractionations between shaded and sunlit leaves could mainly contribute to the model spread in

368    stomatal conductance.

369    Further examination of individual models' features can shed light on the causes of model/site differences in $G_{st}$.

370    The MESSy $G_{st}$ value is strongly governed by LAI followed by soil moisture, and in all other respects MESSy

371    treats different land cover types the same. Therefore, MESSy simulates the highest $G_{st}$ values at PhaDin,

372    Grignion and Mt. Kenya with LAI values of 6.9, 4.3 and 4.2 $m^2 m^{-2}$, respectively (Table 1). In contrast to

373    PhaDin, the high LAI site IT-Cpz (6.9 $m^2 m^{-2}$) experiences significant water stress during summer. This is only

374    captured by MESSy and NOAH indicating higher sensitivity to water stress. During the day, an evident midday

375    depression of $G_{st}$ due to hot weather and water shortage is seen accompanied by a peak in the early morning

376    evident from NOAH, same as has been observed in Mediterranean ecosystems (e.g. Gerosa et al. 2005). The

377    NOAH model accounts for the direct effect of relative humidity on $G_{st}$ (see model description in the supplement)

378    and subsequently modelled a depression in $G_{st}$ at the daily onset (8 am). This variation explains the $G_{st}$ peak at

379    IT-Cpz and Quabbin, which are especially in the summer the two driest among all sites. Due to the dry

380    conditions at the Quabbin site, low soil water and relative humidity, most models, except NOAH, simulate the

381    lowest summer daily mean $G_{st}$ values among all sites. The high estimate by the NOAH model can be explained

382    by the highest $V_{Cmax}$ value among the photosynthesis models (Table 4). The high $g_{max}$ value of 0.55 cm $s^{-1}$ used in

383     Web-DO$_3$SE leading to large estimates is largely dampened by strong soil moisture stress at IT-Cpz (Table S2).

384     Similarly, Web-DO$_3$SE estimates the lowest $G_{st}$ (among the models) values at the Peru site (grassland) due to a

385     strong limitation by the $f_{temp}$ function on stomatal conductance suggesting that the minimum temperature for

386     stomatal opening at 12 °C is too low for these cool temperate conditions. The ZHANG estimates are generally

387     governed by $g_{max}$, explaining the highest and lowest $G_{st}$ values of all models simulated with the ZHANG model

388     at grassland and forest sites, respectively. The CMAQ_J model has the lowest $g_{max}$ values, but it is strongly

389     impacted by soil moisture. The additional dependence of the ZHANG model on solar radiation is reflected in

390     higher $G_{sun}$ relative to $G_{st}$ (Fig. 3 and 4). TEMIR also simulates the smallest spread of $G_{st}$ among the 3 grassland

391     sites (Ambred, MKenya, Peru), as temperature acclimation of photosynthesis (Kattage and Knorr, 2007) is

392     implemented. The different temperatures among the 3 sites have smaller effects on photosynthetic capacity and

393     $G_{st}$ than other models. Despite explicitly considering soil water stress, TEMIR does not capture the impacts of

394     water stress on $G_{st}$ in IT-Cpz and Quabbin in the summer, as the equivalent soil moisture threshold to trigger soil

395     water stress at IT-Cpz and Quabbin is very low (<0.1 m³ m$^{-3}$). Both versions of CMAQ respond very strongly to

396     soil moisture which may not be accurate for each site. The differences between CMAQ-J and CMAQ-P are

397     greatest at the sites with the greatest LAI, such as IT-Cpz and PhaDin.

398
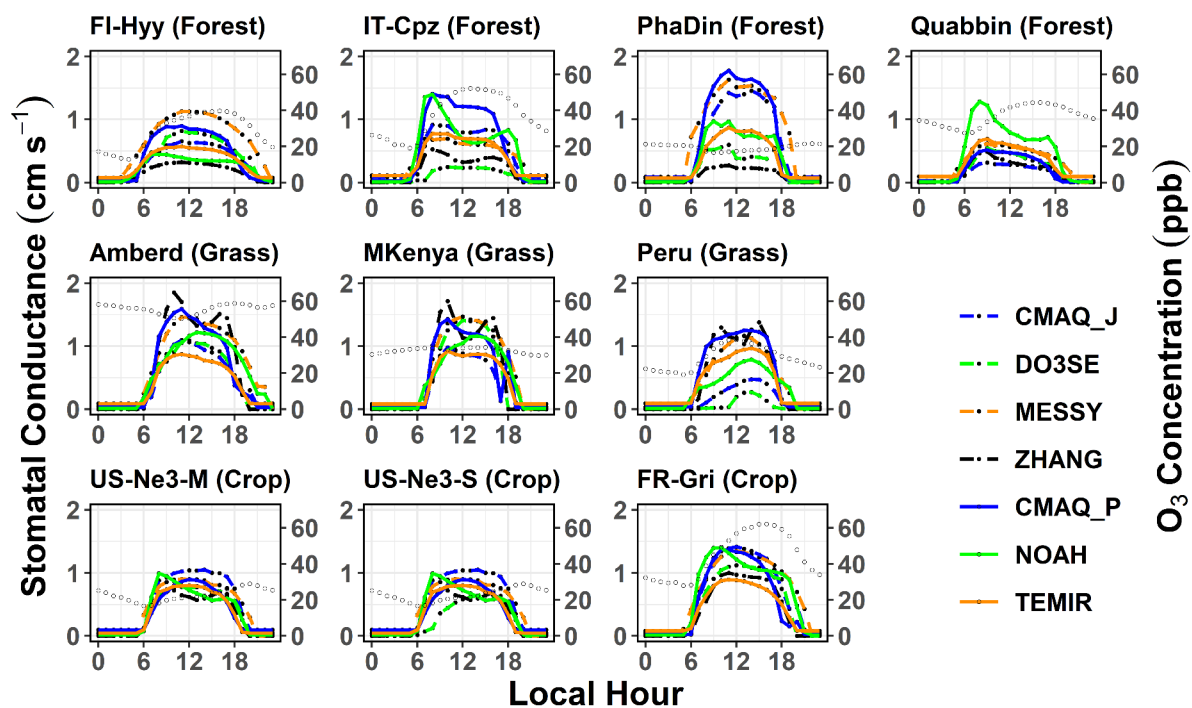
**Fig. 3 Mean diurnal cycle of total stomatal conductance (G$_{st}$) from models across various sites during the**
**summer season (US-Ne3-S=soybeans, US-Ne3-M=maize). Open circles indicate diurnal O$_3$ variations.**
**Respective figures for the other seasons are presented in the supplement.**

399
400
401

402
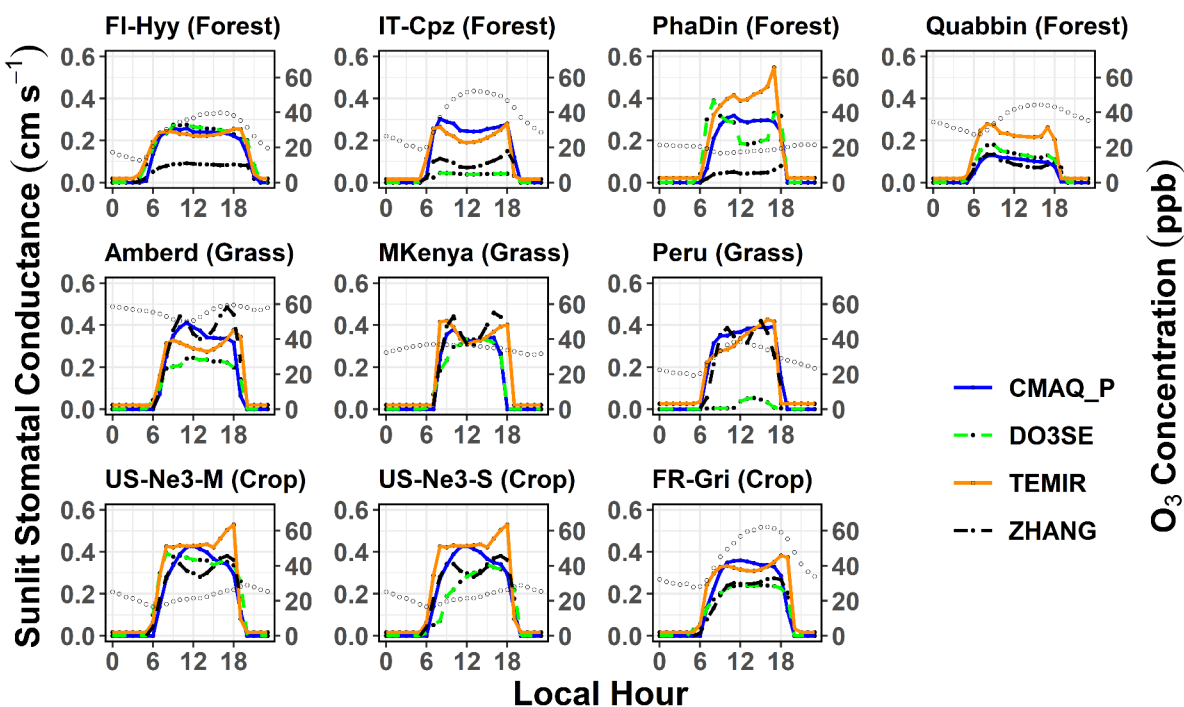
**Fig 4** Mean diurnal cycle of leaf level sunlit stomatal conductance ($G_{sun}$) from the 3 two-leaf models (CMAQ_P, TEMIR, and ZHANG) across various sites during the summer season (US-Ne3-S=soybeans, US-Ne3-M=maize). Open circles indicate diurnal $O_3$ variations. Respective figures for the other seasons are presented in the supplement.

The difference between total and sunlit stomatal flux is examined, and trends of stomatal sunlit flux are characterized by different land cover types and climate conditions. Figures 5 and 6 show the (SRAD>50 Wm$^{-2}$) stomatal $O_3$ flux ($F_{st}$) and stomatal, sunlit $O_3$ flux ($F_{st,sun}$) for different models per season at 9 sites representing forest (top), grass (middle), crops (bottom). Thereby, we consider whether $G_{st}$ and $O_3$ concentration co-variate at diurnal and seasonal timescales. Across all land cover types, a large range of $F_{st}$ (0.05-2 ppb m s$^{-1}$, Fig. 5) is estimated, usually highest in spring and summer and lowest in winter. The largest median of $F_{st}$ is found at Amberd (0.75 ppb m s$^{-1}$; ZHANG, summer), followed by IT-Cpz (0.60 ppb m s$^{-1}$; NOAH, spring), and FR-Gri (0.60 ppb m s$^{-1}$; MESSy and NOAH, summer) owing to both higher $G_{st}$ and $O_3$ concentrations at the respective

417    sites (Fig. 3). Consequently, no general trend can be identified among the sites, i.e flux estimates can differ

418    within one land cover type. Namely, the two crop sites show very different $F_{st}$ estimates (Fig. 5) since they have

419    the most different $O_3$ levels across one land cover type. While the FR-Gri site is exposed to an annual mean $O_3$

420    of 45 ppb (Table S1) as the lowest $O_3$ level of 25 ppb among all sites. The same applies for the diurnal variation

421    of $O_3$ causing either a high (FR-Gri) or a low range (US-Ne3) of flux estimates among all models (in summer

422    and spring). The difference is less apparent in the $F_{st,sun}$ estimates (Fig. 6) which point to the sensitivity of the two

423    leaves to $O_3$ concentration. Similarly, as seen for the stomatal conductance, three of four models show a very

424    good agreement of $F_{st}$ and $F_{st,sun}$ among each other. In terms of seasonality, models agree also generally well

425    among the grassland sites. Among those (and all land cover types), the maximum annual median $F_{st,sun}$ was

426    estimated for Amberd attributed to the high daytime (7 am - 7 pm) annual $O_3$ concentrations (49.3 ppb, Table

427    S1). The most different $F_{st,sun}$ (and $F_{st,sun}$) values are found between the ZHANG (highest) and Web-DO$_3$SE

428    model (lowest) due to the difference in $G_{sun}$ (Fig. 4). Web-DO$_3$SE disagrees the most with the other models and

429    predicts very small fluxes at the Peru site following the small $G_{st}$ and $G_{sun}$ values (Fig. 3 and 4).

430    Among forest sites, spring $F_{st,sun}$ values are comparably high as summer fluxes following the seasonal variation

431    of $G_{sun}$ (Fig. 6, outside the tropics). The highest spring estimates at PhaDin and Quabbin (forests) are linked to

432    the site-specific yearly $O_3$ maximum in this season (Fig. 3). The flux seasonal maximum is more pronounced in

433    all four models (ZHANG, CMAQ_P, TEMIR) when the $O_3$ concentration variation during the year is larger at

434    the respective site. The highest $F_{st,sun}$ (0.1 ppb m s$^{-1}$) is estimated by TEMIR at PhaDin (spring) reflecting the

435    high $G_{sun}$ estimate. In contrast, when considering the total $F_{st}$, CMAQ_P shows the highest estimate (Fig. 5)

436    which indicates that TEMIR uses a higher sunlit fraction than CMAQ_P as it has been shown for stomatal

437    conductance (Fig. 3 and 4). The difference is most apparent at high LAI sites (PhaDin, IT-Cpz, FR-Gri). The

438    lowest estimates of $F_{st,sun}$ (and a very small spread) at the forest sites are shown by the ZHANG model as it has

439    been explained for $G_{st}$ and $G_{sun}$. Overall, CMAQ_P has the lowest spread among the models which was also

440    found in the multi-model comparison study by Clifton et al. (2023).

441

442
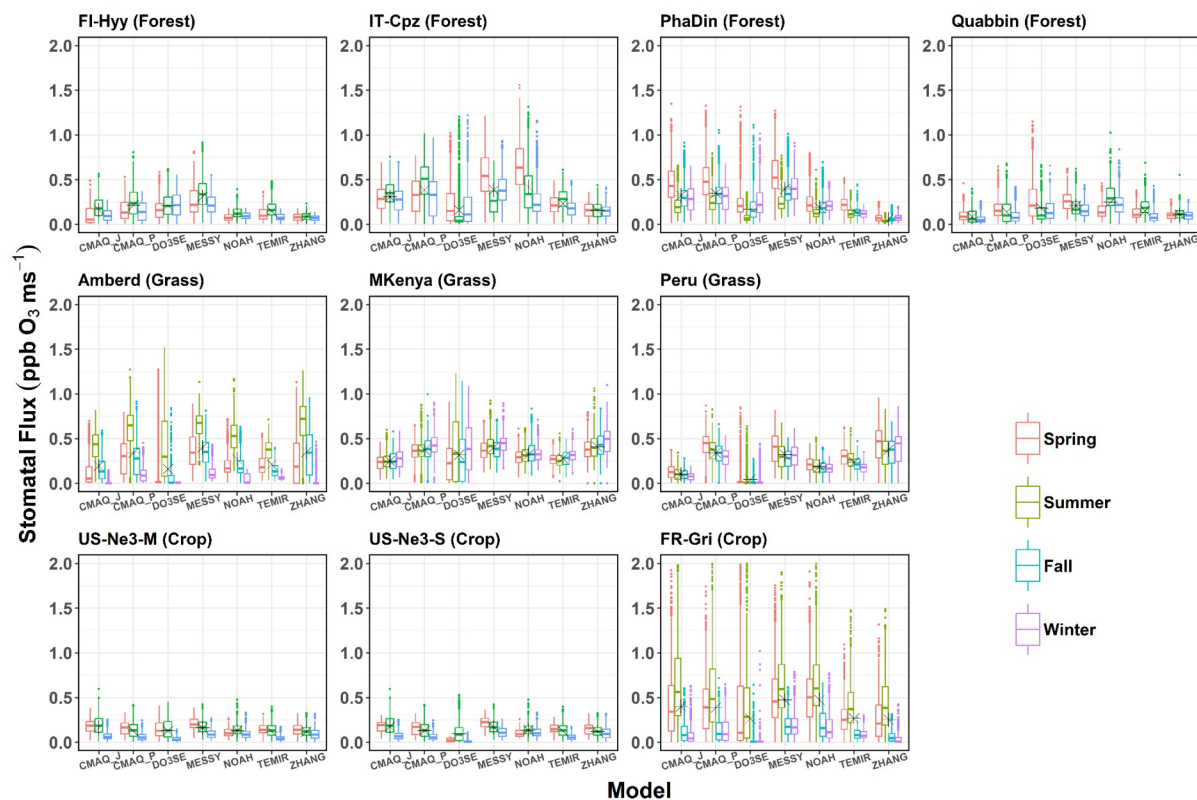
**Fig 5: Boxplots of seasonal mean canopy-level total stomatal O$_3$ flux (ppb ms$^{-1}$) for different models across various sites (data represent SRAD > 50 W m$^{-2}$ and the growing period). Asterisks indicate the annual mean flux**

446    .
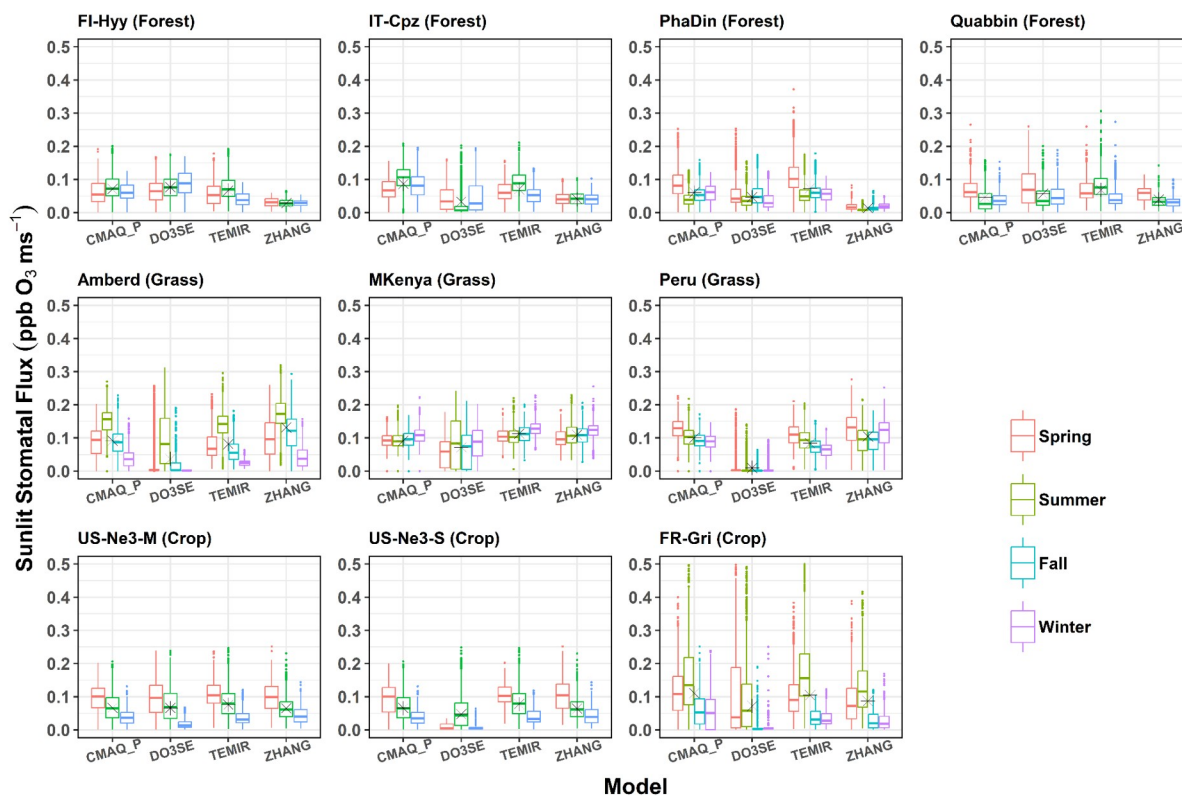
**Fig 6: Boxplots of seasonal mean leaf-level sunlit stomatal $O_3$ flux (ppb ms$^{-1}$) for different models across various sites (data represent SRAD > 50 W m$^{-2}$ and the growing period). Asterisks indicate the annual mean flux.**

### 3.2 Vegetation impact and variation with key input data

This section presents the $POD_y$ calculated from the $O_3$ deposition by different models at 9 different stations to identify trends and patterns of $POD_y$ among land cover types and climates (Fig. 7, corresponding data in Table S9). The critical threshold for ozone damage y differs for the three land cover types. For forests and grass the y value is 1 nmol $O_3$ m$^{-2}$ s$^{-1}$ ($POD_1$) while O3 damage to crops is assumed to occur only when the y threshold exceeds 6 nmol $O_3$ m$^{-2}$ s$^{-1}$ ($POD_6$). By driving the models with changed input data of $O_3$, soil moisture, temperature, relative humidity, growing season (Fig. 8) and with changed $Vc_{max}/g_{max}$ parameter (Fig. 9) we

459 explore the sensitivity of the $POD_y$ estimates. As shown in the previous analysis, the largest $O_3$ uptake and thus

460 the highest $POD_y$ of 28 mmol $O_3$ m$^{-2}$ (on average among all models) is estimated over grassland sites (compared

461 to forest and crops) (Fig. 7). $POD_1$ increases linearly with time for evergreen grasslands whereas Mt. Kenya

462 shows the fastest accumulation (due to the highest $F_{st}$ in spring and summer). Three of the four models lie in a

463 range of 5 mmol $O_3$ m$^{-2}$ whereas Web-DO$_3$SE predicts a maximum $POD_y$ of 10 mmol $O_3$ m$^{-2}$ at all grassland

464 sites. Only at the Peru site, these low values can be reasoned by the significantly lower $G_{sun}$ and $F_{st,sun}$ (compared

465 to other models).

466 For forests, our modelled ensemble $POD_1$ median and maximum values (ranging between 8 and 25 mmol $O_3$ m$^{-2}$) are similar in scale to values estimated across broad geographical regions by other studies. Karlsson et al.

467

468 estimated $POD_1$ values across Europe with the highest values in mid-latitude Europe for coniferous (15 to 20

469 mmol $O_3$ m$^{-2}$) and broadleaf (22 to 28 mmol $O_3$ m$^{-2}$) forests. However, the ZHANG and the Web-DO$_3$SE model

470 are estimated to be significantly lower $POD_1$ than CMAQ_P and TEMIR at each site. These estimates average to

471 16 mmol $O_3$ m$^{-2}$. There is no obvious pattern to which models tend to estimate higher or lower $POD_1$ values, but

472 these estimates are generally consistent with $G_{sun}$ (Fig. 4) and $F_{st,sun}$ (Fig. 6) model estimates explained by

473 particular model constructs or parameterisations. For instance, the ZHANG model estimates low stomatal

474 deposition and thus also $POD_y$ over all forests. Web-DO$_3$SE saw a low $O_3$ uptake only due to the site conditions

475 at IT-Cpz.

476 For crops, the model estimates of $POD_6$ are a little more consistent, with modelled differences within sites only

477 varying between ~ 3 and 11 mmol $O_3$ m$^{-2}$, however, this could in part be due to the overall lower $POD_6$ values

478 due to the use of the higher y threshold. Median model ensemble values range between ~7 and 12 mmol $O_3$ m$^{-2}$

479 across sites. $POD_6$ for staple crops has been estimated in other studies across Europe and globally.  A European

480 study (Schucht et al., 2020) on wheat found $POD_6$ values up to ~ 4 mmol $O_3$ m$^{-2}$ suggesting that our $POD_6$ values

481 for the FR-Gri site tend to be too high. Feng et al. (2012) estimated maximum $POD_6$ values of up to 8 mmol $O_3$

482 m$^{-2}$ for winter wheat in China though these higher values are likely driven by higher ozone concentrations.

483 Similarly, Wang et al. (2022) also found $POD_6$ values for maize of up to 8 mmol $O_3$ m$^{-2}$. Our models give the

484 largest range in $POD_6$ estimates for soybeans at the US-Ne3 site (0 to 11 mmol $O_3$ m$^{-2}$). A key determinant of the

485 range in $POD_y$ simulated by our models, and also with estimates provided in the literature, is the value chosen

486 for $g_{max}$ (or $V_{Cmax}$ depending on the model construct). For example, the multiplicative $g_{sto}$ models used to derive

487 flux-response relationships (see Table 5) use $g_{max}$ values of 450, 126 and 301 mmol $O_3$ m$^{-2}$ s$^{-1}$ for wheat, maize

488    and soybeans (UNECE LRTAP, 2017; Peng et al., 2019 and Zhang et al., 2017). By contrast, our modelling uses

489    a variety of $g_{max}$ values, for example, the Web-DO$_3$SE model uses 450, 305 and 300 mmol O$_3$ m$^{-2}$ s$^{-1}$ for wheat,

490    maize and soybeans. A further consideration in parameter selection are local conditions, a study by Stella et al.,

491    (2013) found a $g_{max}$ value of 296 mmol O$_3$ m$^{-2}$ s$^{-1}$ was most appropriate to describe wheat $g_{sto}$ at the FR-Gri site.

492    This variation highlights the importance of selecting appropriate model parameterisation for conditions, as well

493    as consistency of parameterisation with models used to develop flux response relationships.
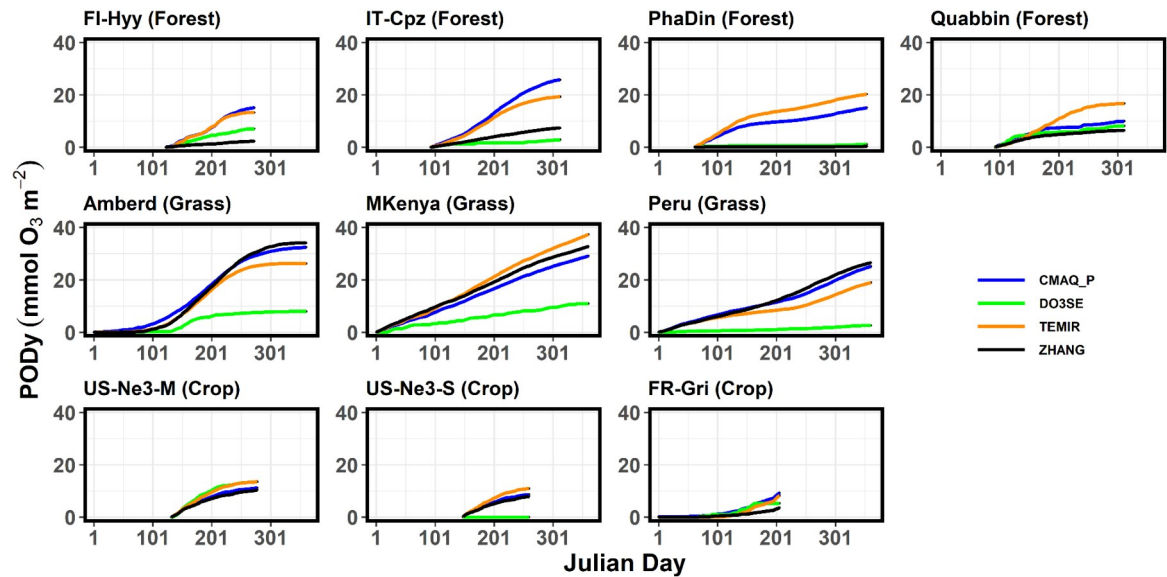
**Fig 7: Evolution of POD$_y$ (mmol O$_3$ m-2) through the growing seasons at various sites.**

494    From the sensitivity analysis, we found that all models show sensitivity of POD$_y$ to changes in O$_3$, specific

495    humidity, and temperature with varying degrees over different land cover types possibly due to different

496    prescribed values such as the temperature threshold (Fig. 8, corresponding absolute values in Table S10).

497    Especially, the POD$_y$ at all sites is most significantly changed when modifying the O$_3$ concentration by +-40 %

498    (Table S11). Crop is the most sensitive land cover to O$_3$ changes across the different models (8.5 mmol m$^{-2}$; 76

499    % POD$_y$ change with respect to the base run), followed by forest (10.0 mmol O$_3$ m$^{-2}$; 59.3%) and grass (14.9

500    mmol O$_3$ m$^{-2}$; 56.1%) which is due to the plant physiognomy (Grulke and Heald et al. ,2020). In a relative sense,

501    the average response change in POD$_y$ to a 40 % change in O$_3$ concentrations is the greatest in ZHANG (+9.2

502   mmol $O_3$ m$^{-2}$, corresponding to a 68.1 % $POD_y$ change with respect to the base run), followed by CMAQ_P and

503   TEMIR (12 and 11.9 mmol $O_3$ m$^{-2}$ ;64.8 % and 63.5 %), and then by Web-DO$_3$SE (11.4 mmol $O_3$ m$^{-2}$; 53.0 %).

504   Also, the $POD_y$ estimate seems to be sensitive to humidity (Q) changes (+-30%) among all models. At forest, the

505   $POD_y$ estimates appear to be the most sensitive (4.6 mmol $O_3$ m$^{-2}$; 27.3%), followed by crops (2.9 mmol $O_3$ m$^{-2}$;

506   25.9%) and grass (4.6 mmol $O_3$ m$^{-2}$; 17.3 %). The response is the greatest in TEMIR and CMAQ (between 5.7

507   and 6.7 mmol $O_3$ m$^{-2}$; 30.7-35.8 %), while it is much smaller for ZHANG (usually close to zero on average). The

508   most non-linear response was shown by Web-DO$_3$SE at IT-Cpz which estimated a 5 times higher $POD_y$ response

509   to increasing humidity than to a humidity decrease pointing towards the strong dryness at this site limiting   If

510   temperature is changed by +-3 K the highest sensitivity was found at crops on average (2.7 mmol $O_3$ m$^{-2}$;

511   24.1%), followed by grass (4.6 mmol $O_3$ m$^{-2}$; 17.2 %) and forest (1.6 mmol $O_3$ m$^{-2}$; 9.5%). The responses

512   unevenly vary in sign depending on the model because the temperature change depends on the optimal

513   temperature at the specific sites. Namely most models estimate a $POD_y$ decrease when increasing temperature

514   (Fig. 5). As described in Hayes et al. (2019), a temperature increase is seen in southern countries where

515   temperature could limit stomatal uptake since temperature is already close to the optimum in normal conditions.

516   From our sensitivity analysis, temperature impacts on $POD_y$ are noticeable only for a few sites (e.g., Ambered,

517   Mt. Kenya, and Peru) and models's response to $POD_y$ change were different due to different thresholds used for

518   the temperature stress factors to stomatal conductance. The greatest changes in magnitude are predicted by Web-

519   DO$_3$SE (5.1 mmol $O_3$ m$^{-2}$; 23.7%), followed by CMAQ_P (3.1 mmol $O_3$ m$^{-2}$; 16.7%), ZHANG (1.9 mmol $O_3$ m$^{-2}$;

520   14.1 %) and TEMIR (1.7 mmol $O_3$ m$^{-2}$; 9.6 %). In contrast, not all models are sensitive to changes of soil water

521   content (SWC). The greatest response is seen in CMAQ_P (-6.3 and +1.4 mmol m$^{-2}$; -34.0% and +7.6%),

522   followed by Web-DO$_3$SE (-2.2 and -2.2 mmol m$^{-2}$; -10.2% and -10.2%), and TEMIR (-1.1 and +0.8 mmol $O_3$

523   m$^{-2}$ ; -5.9% and +4.3%), while ZHANG shows no difference in this regard because it is not sensitive to soil

524   moisture. The changes are largest at crops (1.5 mmol $O_3$ m$^{-2}$; 13.4%), while grass and forest show similar

525   responses (2.8 and 1.7 mmol $O_3$ m$^{-2}$; 10.5 and 10.1 %, respectively). That is in line with De Marco et al. (2020)

526   who show that $POD_y$ responses to soil water changes increase with higher Y threshold (here crops). The models

527   do not appear to be sensitive to LAI 14d shifts, with the only exception of Web-DO$_3$SE, which simulates a lower

528   $POD_y$ for both early and late LAI shifts (-2.6 mmol $O_3$ m$^{-2}$ on average, across all land covers). LAI is used as a

529   proxy for growing seasons in most models whereasWeb-DO$_3$SE considers growing seasons directly.

530

**531**
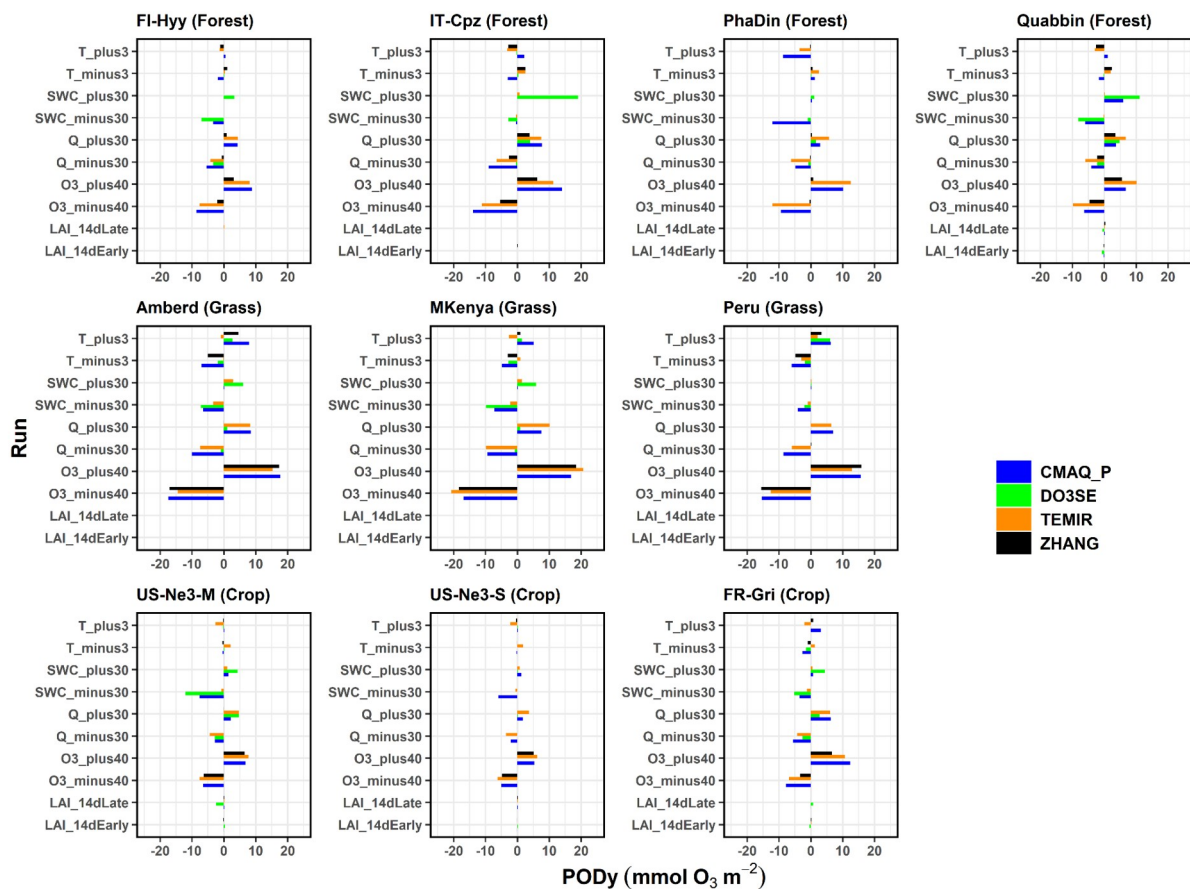
**Fig 8: Meteorology sensitivity assessment: Absolute change of POD$_y$ values with respect to Base run POD$_y$ due to 10 or 20 % variation of the temperature (T), soil water content (SWC), absolute humidity (Q), O$_3$ and LAI/growing season.**

**535**

**536** A 20% change of g$_{max}$/Vc$_{max}$ leads to corresponding changes in POD$_y$ values. An increase or decrease of the

**537** parameter leads to very similar changes (in +-) (Fig. 9, corresponding data in Table S12 – S14). The response

**538** appears to be generally uniform across sites. On average, the results show +28.9 ± 22.4 % POD$_y$ change for the

**539** 20 % increase of g$_{max}$/Vc$_{max}$, and -27.4 ± 13.1 % for the 20 % decrease with the largest absolute changes at

**540** grassland (up to 8 mmol O$_3$ m$^{-2}$ , ZHANG). At forests and crops, changes up to 5 and 3 mmol O$_3$ m$^{-2}$ occur,

541  respectively. Among all sites, noticeably higher (the highest) relative changes were estimated at FR-Gri which

542  thus constituted the only relevant source of variability. This change is significantly different to the change at US-

543  Ne3 (20-30 %) which reflects the contrasting low $O_3$ level at US-Ne3 compared to the highly polluted FR-Gri

544  site. Also, the ZHANG model predicts the highest changes at crops while CMAQ_P seems insensitive. The

545  ZHANG (and TEMIR) model appears to be the most sensitive model to the changes at most sites due to the

546  strong dependency on the $g_{max}/Vc_{max}$ parameter (see analysis above). The only climate trend of the response is

547  seen by the ZHANG model which shows an average 65 % increase/decrease in wet forests (PhaDin, FI-Hyy) and

548  only a 40 % change in dry places. Sites with very low estimates (PhaDin in ZHANG, Peru in Web-DO$_3$SE) were

549  excluded from this sensitivity study.

550

551
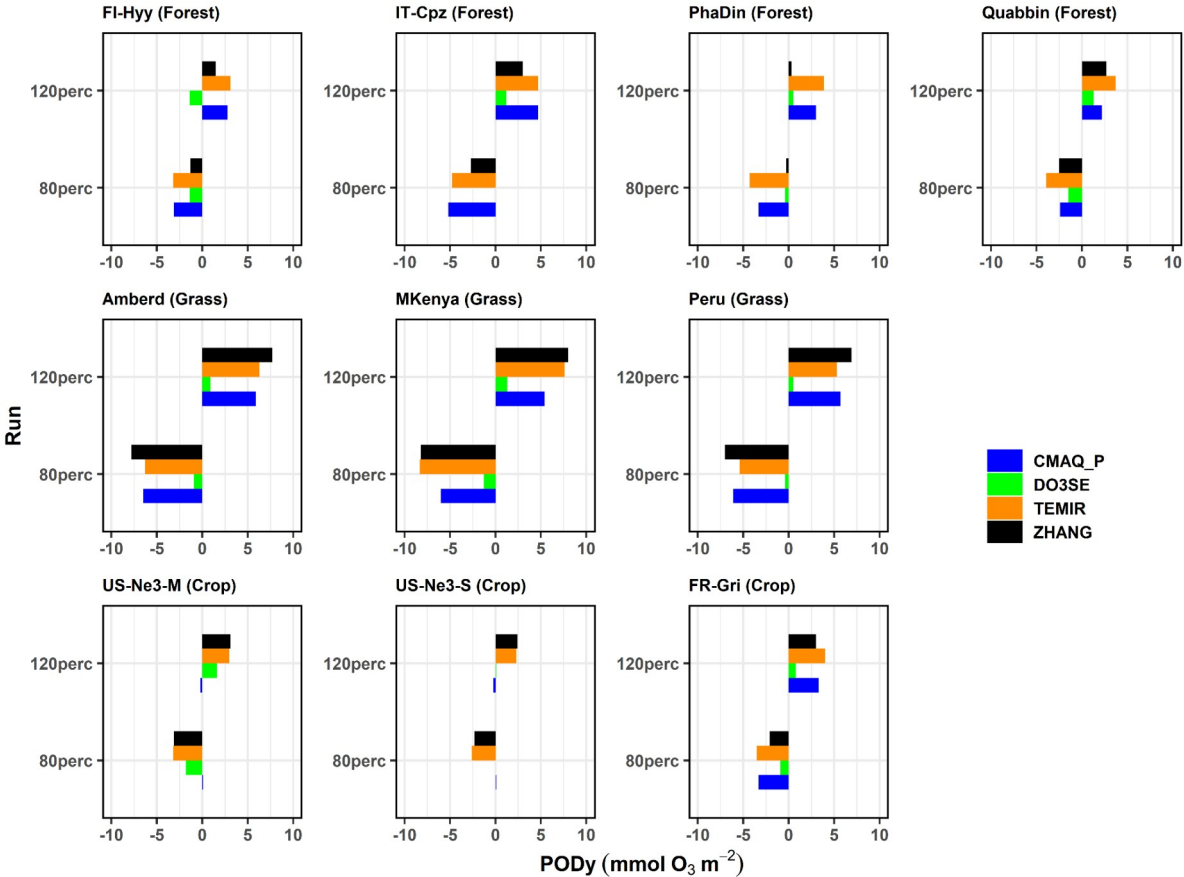
**Fig 9: Land cover parameterisation sensitivity assessment: Absolute change of $POD_y$ values with respect to the base run $POD_y$ values due to 20 % variation of $G_{max}$ or $V_{Cmax}$.**

To indicate the likely damage, and range of damage that our modelled values of $POD_y$ predict, we have used $POD_y$ flux-response relationships available in the literature that most closely represent the vegetation type and climatic location of each study site (Table 5). To estimate $O_3$ damage to forests we use recently derived flux-response relationships that relate $POD_1$ values to gross annual increment (Karlsson et al., sub) and hence indicate the annual change in growth rate caused by $O_3$. The mean model ensemble estimates a percentage reduction in gross annual increment of around 5% for FI-Hyy and Pha Din, 6% for IT-Cpz and 14% for Quabbin. However, the range in estimates across models is not insignificant and most extreme at the Quabbin site with a minimum of 11% and a maximum of 21% around the mean 13% value; this is due to broadleaf deciduous species being more sensitive to $O_3$ dose than needleleaf species and hence more sensitive to a range of $POD_y$ model simulations (Bueker et al., 2015). It should also be emphasised that the Pha Din site uses a European-derived flux-response relationship for an Asian forest site.

| Site | Species | y | Flux-response relationship | Response metric & species | PODy | | | % Response | | | Location of PODy relationship | Reference |
|---|---|---|---|---|---|---|---|---|---|---|---|---|
| | | | | | min | median | max | min | median | max | | |
| FI-Hyy | Scots pine | 1 | y = -0.0057x + 1.0015 | Gross Annual Increment (GAI) % for Norway spruce/Scots pine | 2.3 | 10.2 | 15.1 | 1.2 | 5.6 | 8.5 | Europe | Karlsson et al., sub (to TOARII community special issue) |
| Quabbin | Birch/ Beech (Broadleaf deciduous) | 1 | y = -0.0093x + 0.9461 | Gross Annual Increment (GAI) % for Birch/Beech | 6.5 | 9.1 | 16.8 | 11.4 | 13.9 | 21.0 | Europe | Karlsson et al., sub (to TOARII community special issue) |
| PhaDin | Norway spruce (Evergreen needleleaf) | 1 | y = -0.0057x + 1.0015 | Gross Annual Increment (GAI) % for Norway spruce/Scots pine | 0.4 | 8.1 | 20.3 | 0.0 | 4.5 | 11.4 | Europe | Karlsson et al., sub (to TOARII community special issue) |
| IT-Cpz | Holm oak | 1 | y = -0.0047x + 1.001 | Gross Annual Increment (GAI) % for Aleppo pine/Holm Oak | 2.8 | 13.3 | 25.8 | 1.2 | 6.2 | 12.0 | Europe | Karlsson et al., sub (to TOARII community special issue) |
| FR-Gri | winter wheat | 6 | y = -0.0385x + 1.003 | % grain yield loss for wheat | 3.6 | 6.8 | 9.3 | 13.6 | 25.9 | 35.5 | Europe | UNECE LRTAP Mapping Manual (2017) |
| US-Ne3 (Maize) | Maize | 6 | y=0.0426x+1 | % grain yield loss for wheat | 10.5 | 12.4 | 13.6 | | | | | Peng, J., Shang, B., Xu, Y., Feng, Z., Pleijel, H. and Calatayud, V., 2019. Ozone exposure-and flux-yield response relationships for maize. Environmental pollution, 252, pp.1-7. |
| US-Ne3 (Soybean) | Soybean | 6 | y = -0.033x + 1.01 | % relative seed yield loss per soybean plant | 0.0 | 8.3 | 11.0 | 0.0 | 26.4 | 35.3 | China | Zhang, W., Feng, Z., Wang, X., Liu, X., Hu, E. (2017) Quantification of ozone exposure-and stomatal uptake-yield response relationships for soybean in Northeast China. Sci of the Total |

69
70
71

| | | | | | | | | | | | | | |
|---|---|---|---|---|---|---|---|---|---|---|---|---|---|
| | | | | | | | | | | | | Env., (710-720) | 599-600 |
| Amber d | Grassland | 1 | y = -0.0062x + 0.947 | % total biomass loss for temperate perennial grassland | 7.9 | 29.4 | 34.1 | 10.2 | 23.5 | 26.4 | Europe | UNECE Mapping (2017) | LRTAP Manual |
| MKenya | Grassland | 1 | y = -0.0062x + 0.947 | % total biomass loss for temperate perennial grassland | 10.9 | 31.0 | 37.4 | 12.1 | 24.5 | 28.5 | Europe | UNECE Mapping (2017) | LRTAP Manual |
| Peru | Grassland | 1 | y = -0.0062x + 0.947 | % total biomass loss for temperate perennial grassland | 2.6 | 22.1 | 26.6 | 6.9 | 19.0 | 21.8 | Europe | UNECE Mapping (2017) | LRTAP Manual |

**Table 5. Estimates of O$_3$ damage (for specific response metrics) derived from using the ensemble mean modeled PODy values (and minimum and maximum values) with appropriate flux-response relationships based on land cover type. The climatic location within which the flux-response relationships are derived are stated to show the relevance of their use in estimating damage. Shaded cells denote flux-response relationships that are derived outside of the broad climate region to which they are applied in this study and hence whose damage estimates should be treated with caution.**

For crops, flux response relationships are available for wheat, maize and soybeans (UNECE LRTAP, 2917, Peng et al., 2019 and Zhang et al., 2017). These relationships are derived from Europe (wheat) and China (maize and soybean). For wheat, we see a large range in percentage yield loss with a mean model ensemble of 26 % but a maximum yield loss of 35 %. This is driven by high POD$_6$ values derived from CMAQ_P and TEMIR. For maize at US-Ne3 the results are very consistent with relative grain yield loss estimates ranging from 1.4 to 1.6 %. For soybeans at US-Ne3, the results are less consistent than maize with a minimum and maximum of 0 and 35 % yield around a mean of 26 %. It is important to note that a Chinese-derived flux-response relationship is used to estimate O$_3$ damage on both US-grown crops.

72
73
74

584  Finally, for grasslands, we estimate total biomass losses of 19, 24 and 23% from the ensemble model mean for Peru, Mt

585  Kenya and Amberd respectively. The range in model values is relatively small for Amberd and Mt Kenya. A low minimum

586  value of 6 % total biomass loss is estimated for Peru due to the Web-DO$_3$SE model having a very low POD$_y$ at this location

587  due to a likely oversensitive limitation to O$_3$ uptake caused by low temperatures.

588

## 4. Discussion and Conclusion

590  Here we have compared six deposition schemes commonly used in atmospheric chemistry transport models. We have

591  focussed on the stomatal component of deposition since this is acknowledged to have a substantial influence on damage to

592  vegetation, and ultimately the ability of these six models to estimate the POD$_y$ metric designed to indicate the level of O$_3$

593  damage to forest, crops and grasslands. The models estimate POD$_y$ values of 28, 15 and 9 mmol O$_3$ m$^{-2}$ for grassland, forests

594  and crops, respectively. The multi-model mean estimates are generally in the expected range which suggests that the

595  stomatal flux output of these models could be used for O$_3$ impact assessments. We also explored the differences in POD$_y$ by

596  geographical location. When comparing one vegetation type, we find multiple drivers including O$_3$ concentration. The

597  different model types are not the driving force, instead, the models can predict similar results.

598  There are three key reasons for differences in dry deposition model estimates i. model construct and the inclusion/exclusion

599  of important factors that determine G$_{st}$ and G$_{sun}$; ii. model parameterisation which may characterise the land cover types and

600  iii. differing model sensitivity to climate variables (seasonal, location effects) in estimates of stomatal deposition. The model

601  comparison of stomatal conductance and stomatal dry deposition for ozone helps us to understand the differences between

602  models. We found that models simulate generally reasonable stomatal deposition of 0.5 -0.8 cm s$^{-1}$ in summer whereas the

603  different model types often agree very well with each other. The stomatal conductance estimates among the models agree

604  with correlation coefficients of 0.75, 0.80 and 0.85 for forests, crops and grasslands. Thereby, the 9 sites selected for this

605  study also reflect different climate conditions; however the selection of sites that provide such broad representations also

606  means that the analysis and the results cannot be generalized. The global coverage, diverse land types and varying

607  meteorological conditions of the 9 sites resulted in widespread model responses to soil moisture (Fig. 8), while appearing to

608  be insensitive to changes of LAI (Fig. 9). The former underscored the idiosyncratic features and hence potential limitations

609  of individual models, whereas the latter gave us confidence in model capabilities despite the different constructs and

610  parameterizations of the models. The model differences, identified during this analysis, can be explained by the model's

611  dependence on the meteorological conditions at sites. Indeed, both model structure (e.g. Raghav, Kumar and Liu 2023) and

612  parameters (Fares et al., 2013) can affect the accuracy of stomatal conductance models. However, studies have shown that

613  when properly calibrated against field observations, structurally different stomatal models can produce similar stomatal

614 conductance (Fares et al., 2013, Mäkela et al., 2019). Calibrating the key parameters of stomatal conductance models (e.g.

615 $g_{max}/Vc_{max}$) is a crucial next step to improve the accuracy of stomatal conductance and $POD_y$ estimates, as our sensitivity tests

616 show direct, and possible non-linear relationship between $POD_y$ and $g_{max}/Vc_{max}$ (e.g. at FR-Gri). This is possible with the

617 recent availability of standardised global eddy flux (FLUXNET, Pastorello et al., 2020) and sap flow (SAPFLUXNET,

618 Poyatos et al., 2020) data.

619 To estimate $POD_y$ for a representative leaf of the upper canopy, the sunlit leaf must be distinguished from the total leaf.

620 Since the effects-based community recognised that sunlit leaves contribute most to carbon assimilation throughout the

621 growing season or $O_3$ sensitive period (e.g. in wheat, this is considered to be the time from anthesis to maturity) and hence it

622 will better represent damaging $O_3$ uptake. All flux response relationships for $POD_y$ are developed for such a representative

623 leaf. This is an important distinction since previous model comparison studies (e.g.Clifton et al., 2023) have tended to focus

624 on whole canopy dynamics. These are important to estimate accurately, but to estimate $POD_y$ requires additional canopy

625 level processes, which need i. $O_3$ concentration at the top of the canopy, ii. wind speed at the top of the canopy and iii. $G_{sun}$ of

626 a representative leaf at the top of the canopy. Studies (Emberson 2020 and references therein) have established thresholds for

627 different land cover types which are used to provide y values for the selected sites with specific land cover types in this

628 study. Some studies suggest that the y threshold for land cover types may vary by global region (e.g. a number of studies

629 suggest higher y values of up to 12 nmol $O_3$ $m^2$ $s^{-1}$ is more appropriate for crops and forest tree species in Asia). In this study,

630 which focuses on comparing across models, we maintain consistency and use common y threshold values for each land

631 cover type. However, this is an aspect that would benefit from further study in the future since estimating PODy values with

632 higher thresholds is more challenging for all types of model given the less frequent occurrences of such high $O_3$ doses.

633 Our models estimate 30-50 % of stomatal $O_3$ deposition at sunlit leaves. Thereby, the model estimates of the total stomatal

634 flux are more widespread (during one season) than the estimates of the sunlit only which suggests an important role of the

635 model's partitioning in two big leaves. When calculating $POD_y$ model means estimates generally agree with the literature but

636 most discrepancies between model estimates of $POD_y$ ultimately come down to the differences in simulations of stomatal

637 conductance. The sensitivity analysis of $POD_y$ yields ozone as the most important input variable, to whose changes all

638 models respond similarly. Considering all models and sites together, $POD_y$ were affected most by the $O_3$ concentration (+-

639 60-80 % site-dependent, i.e., higher $O_3$ concentration leads to higher $POD_y$), followed by humidity (30-50 % site-dependent

640 impact). Soil moisture impacts were also significant for the CMAQ_P and Web-DO$_3$SE model (up to +-68 % and 22 %

641 change). The sensitivity to temperature changes varies strongly among the model and its parametrization. As the plant

642 canopy acts as a persistent sink of $O_3$, there is a significant vertical gradient of $O_3$ within the atmospheric surface layer. For

643 example, Travis et al. (2019) show that the midday $O_3$ concentration at 65 m above ground (mid-point of a first vertical layer

644 of GEOS-Chem v9-02) is 3 ppb higher than the $O_3$ concentration at 10 m above ground (inferred by Monin-Obukhov

645 Similarity Theory, MOST) over the Southeastern United States. A mismatch between $O_3$ measurement height and canopy

78
79
80

height can lead to inaccurate $POD_y$ calculation (Gerosa et al, 2017). An O3 bias of 2 ppb as estimated by e.g. Tarasick et al. (2018) would lead to a change of 6-7 % in POD1 (Gerosa et al., 2017). Similarly, we show that the errors in $O_3$ concentrations propagate non-linearly to $POD_y$ (i.e. 40% changes in $O_3$ leads to 53 - 68 % changes in $POD_y$), such a mismatch should be carefully avoided by applying atmospheric surface layer theories (e.g. MOST) to estimate the vertical profile of $O_3$, and therefore the canopy-top $O_3$ concentration, if direct measurement or model output of $O_3$ at canopy top is not available.

Finally, we use flux-response relationships for temperate deciduous (Beech/birch), temperate needleleaf (Norway spruce (*Picea abies*)), crops (wheat (*Triticum aestivum)*, maize (*Zea mays*) and soybeans (*Glycine max*)) and grassland (*Lolium perenne*) to give a suggest the potential likely variation of damage estimates by land cover type and climatic region. These relationships have predominantly been developed for European and Asia forest and crop species. Therefore, they should be applied to other climate regions with caution although recent evidence suggests that tropical forest species may have similar sensitivity to $O_3$ as European species (Cheeseman et al. 2024). Although there is rather large variability in $POD_y$ values estimated by the model, the median values are relatively robust. Unfortunately, there is only statistical or modelled evidence of actual $O_3$ damage, and only at a few of the sites investigated. Modelled evidence uses stomatal ozone flux models similar to those used in this study, but which have been parameterised for local site conditions (Stella et al., 2013 for FR-Gri wheat). Simulations with a terrestrial biosphere model suggested an average long-term $O_3$ inhibition of 10.4% for the period 1992– 2011 at the Harvard site (Yue et al 2016); this compares to our model ensemble estimate of 14% GAI biomass loss for Quabbin. A significant but small NEP reduction was found during Spring in the Italian Castelporziano forest site (up to -1.37 %) but not at the FI-Hyy or FR-Gri sites (Savi et al., 2020). Our modelling estimated substantially lower $POD_y$ values and associated damage at Hyy and IT-Cpz than Quabbin though we would expect to see a more substantial $O_3$ effect than that demonstrated by the NEP statistical modelling (i.e. 5 and 6% GAI biomass loss at FI-Hyy and IT-Cpz respectively). Similar simulations with a different terrestrial biosphere model found only moderate $O_3$ damage effects (GPP reductions of 4–6 %; Yue & Unger, 2014). This result is driven by low ambient ozone concentrations but also by the choice of a C4 photosynthetic mechanism to estimate stomatal conductance which gives relatively high-water use efficiency). These simulations also suggested that the US-Ne3 experienced a higher ozone effect on GPP than Harvard which is consistent with our modeling for soybeans (but not maize, generally considered an $O_3$ tolerant crop species; Mills et al 2011). According to the $POD_6$ estimates made using a SURFATM model, parameterised for Grignon wheat, $POD_6$ values of 1.094 mmol $O_3$ $m^{-2}$ were estimated from 1 April to 1 July 2009 which compared with our range of 3.6 to 9.3; the locally parameterised values gave estimated crop yield losses of 4.2%, compared to our median model ensemble estimates of 25% for the winter wheat. This is most likely due to the lower $g_{max}$ value used in the local parameterisation (296 mmol $O_3$ $m^{-2}$ $s^{-1}$). However, no

81
82
83

677 recording of actual damage is given at the FR-Gri site, so it is not possible to tell which of these simulated damage estimates
678 is closer to reality.

679 The experiments performed here with varying climate and vegetation input data also find a similar sensitivity of $POD_y$ to $O_3$.
680 It is helpful to have a range of models and model constructs in deposition schemes especially where these have been
681 developed for particular land cover types. When used in damage estimates it is important to ensure that key stressors are
682 included which may be important for that respective geographical region (such as soil and vapour pressure deficit).
683 Recognising that several deposition schemes would be able to reliably predict $POD_y$ for different climates and cover types
684 once they have been parameterised appropriately will extend the usefulness of flux-response relationships.

685 Overall, this study has demonstrated the widespread applicability and consensus among various numerical stomatal flux
686 methods. Both semi-mechanistic as well as empirical models can generally represent observed ozone fluxes among different
687 land cover types and climates. We identified the key model constructs and parameterisations that cause differences in $POD_y$
688 estimates. However, none of the models clearly shows a superior overall performance. Instead, all models can be effectively
689 applied, each with its own strengths and weaknesses. Our findings present exciting opportunities to extend applications
690 beyond specific sites and growing seasons, enabling comprehensive global stomatal flux studies over longer periods.
691 Integrating the TOAR database with the Web-DO$_3$SE model enables automatic model runs for ozone-vegetation impact
692 assessment at a large range of sites using the TOAR database.

693
694
### Author contributions
696 T.E.: site selection, TOAR data extraction, data preparation, model support, modelling Web-DO$_3$SE, writing, coordination.
697 A.M.: modelling (ZHANG, MESSy, NOAH-GEM, TEMIR model), statistics, plots and analysis. L.E.: concept, writing.
698 H.M.: writing, reviewing. L.Z.: concept and writing. L.R: modelling with CMAQ, FLUXNET data preparation. C.B.:
699 debugging and test simulations of Web-DO3SE. A.W.: site selection, preparation of FLUXNET and sensitivity data. G.K.:
700 site selection, TOAR data extraction. G.G.: site analysis. M.H.: plots and reviewing. P.G.: PODy analysis.
701
### Competing interests
703 The authors have no competing interests.
704

### Acknowledgements
706 We acknowledge the TOAR team supporting the data extraction. The authors acknowledge the access to the meteorological
707 data on the Jülich MeteoCloud provided by Jülich Supercomputing Centre (Krause et al., 2018). Tamara Emmerichs thanks

708    the German Research Foundation as part of the CLICCS Clusters of Excellence (DFG EXC 2037). We thank the responsible

709    people of the selected measurement sites for their support in obtaining site information. We greatly appreciate helpful

710    discussions in the earlier stages of the project from the following people: Owen Cooper, Zhaozhong Feng, Laurens

711    Ganzeveld, Meiyun Lin, Martin Schultz, Eran Tas, and Oliver Wild.

712

**Code availability**

714    The Web-DO$_3$SE source code is freely available at https://toar-data.fz-juelich.de/ under the CC-BY 4.0 license

715    (https://creativecommons.org/licenses/by/4.0/). The further model code can be obtained upon request.

716

**Data availability**

718    The TOAR data is freely available at https://toar-data.fz-juelich.de/ under the CC-BY 4.0 license

719    (https://creativecommons.org/licenses/by/4.0/). The ERA5 data used can be downloaded from the MeteoCloud server

720    (https://datapub.fz-juelich.de/slcs/meteocloud/index.html). FLUXNET 2015 dataset is publicly available at

721    https://fluxnet.org/data/fluxnet2015-dataset/. Stomatal conductance estimates, and the related FLUXNET 2015 data from

722    SynFlux version 2 can be obtained by contacting Christopher Holmes (cdholmes@fsu.edu). The model outputs are available

723    from Zenodo (DOI: 10.5281/zenodo.15812487).

724

## References

726    Ainsworth, E. A., Yendrek, C. R., Sitch, S., Collins, W. J., and Emberson, L. D.: The effects of tropospheric ozone on net

727    primary productivity and implications for climate change. Annual review of plant biology, 63(1), 637-661,

728    https://doi.org/10.1146/annurev-arplant-042110-103829, 2012.

729

730    Ainsworth, E. A.: Understanding and improving global crop response to ozone pollution. The Plant Journal, 90(5), 886-897,

731    https://doi.org/10.1111/tpj.13298, 2017.

732

733    Avnery, S., Mauzerall, D. L., Liu, J., and Horowitz, L. W.: Global Crop Yield Reductions due to Surface Ozone Exposure: 1.

734    Year 2000 Crop Production Losses and Economic Damage, Atmos. Environ., 45, 2284–2296,

735    https://doi.org/10.1016/j.atmosenv.2010.11.045, 2011.

736

737    Aguilos, M., Hérault, B., Burban, B., Wagner, F., & Bonal, D.: What drives long-term variations in carbon flux and balance

738    in a tropical rainforest in French Guiana?. Agricultural and forest meteorology, 253, 114-123,

739    https://doi.org/10.1016/j.agrformet.2018.02.009, 2018.

740

741 Amos, B., Arkebauer, T. J., and Doran, J. W.: Soil surface fluxes of greenhouse gases in an irrigated maize-based

742 agroecosystem. Soil Science Society of America Journal, 69(2), 387-395, https://doi.org/10.2136/sssaj2005.0387, 2015.

743

744 Beck, H. E., McVicar, T.R., Vergopolan, N. Berg, A., Lutsko, N. J., Dufour, A., Zeng, Z., Jiang, X., van Dijk, A. I. J. M.,

745 and Miralles, D. G.: High-resolution (1 km) Köppen-Geiger maps for 1901–2099 based on constrained CMIP6 projections.

746 Sci Data 10, 724, https://doi.org/10.1038/s41597-023-02549-6, 2023.

747

748 Broberg, M. C., Feng, Z., Xin, Y.,and Pleijel, H.: Ozone effects on wheat grain quality–A summary. Environmental

749 Pollution, 197, 203-213, https://doi.org/10.1016/j.envpol.2014.12.009, 2015

750

751 Büker, P., Feng, Z., Uddling, J., Briolat, A., Alonso, R., Braun, S., Elvira, S., Gerosa, G., Karlsson, P.E., Le Thiec, D. and

752 Marzuoli, R., 2015.: New flux based dose–response relationships for ozone for European forest tree species. Environmental

753 Pollution, 206, pp.163-174. https://doi.org/10.1016/j.envpol.2015.06.033 , 2015.

754

755 Bukowiecki, N., Steinbacher, M., Henne, S., Nguyen, N.A., Nguyen, X.A., Hoang, A.L., Nguyen, D.L., Duong, H.L.,

756 Engling, G., Wehrle, G., Gysel-Beer, M. and Baltensperger, U.: Effect of Large-scale Biomass Burning on Aerosol Optical

757 Properties at the GAW Regional Station Pha Din, Vietnam. Aerosol Air Qual. Res. 19: 1172-1187, https://doi.org

758 /10.4209/aaqr.2018.11.0406, 2019.

759

760 Clifton, O. E., Fiore, A. M., Munger, J. W., and Wehr, R.: Spatiotemporal controls on observed daytime ozone deposition

761 velocity over northeastern US forests during summer. Journal of Geophysical Research: Atmospheres, 124(10), 5612-5628,

762 https://doi.org /10.1029/2018JD029073, 2019.

763

764 Clifton, O. E., D. L. Lombardozzi, A. M. Fiore, F. Paulot, and L. W. Horowitz.: Stomatal conductance influences interannual

765 variability and long-term changes in regional cumulative plant uptake of ozone. Environmental Research Letters.

766 https://doi.org /10.1088/1748-9326/abc3f1, 2020a.

767

768 Clifton, O. E., Paulot, F., Fiore, A. M., Horowitz, L. W., Correa, G., Baublitz, C. B., ... and Weng, E.: Influence of dynamic

769 ozone dry deposition on ozone pollution. Journal of Geophysical Research: Atmospheres, 125(8),

770 https://doi.org /10.1029/2020JD032398, 2020b.

771

Clifton, O. E., Schwede, D., Hogrefe, C., Bash, J. O., Bland, S., Cheung, P., Coyle, M., Emberson, L., Flemming, J., Fredj, E., Galmarini, S., Ganzeveld, L., Gazetas, O., Goded, I., Holmes, C. D., Horváth, L., Huijnen, V., Li, Q., Makar, P. A., Mammarella, I., Manca, G., Munger, J. W., Pérez-Camanyo, J. L., Pleim, J., Ran, L., San Jose, R., Silva, S. J., Staebler, R., Sun, S., Tai, A. P. K., Tas, E., Vesala, T., Weidinger, T., Wu, Z., and Zhang, L.: A single-point modeling approach for the intercomparison and evaluation of ozone dry deposition across chemical transport models (Activity 2 of AQMEII4), Atmos. Chem. Phys., 23, 9911–9961, https://doi.org /10.5194/acp-23-9911-2023, 2023.

Chen, X., Quéléver, L. L. J., Fung, P. L., Kesti, J., Rissanen, M. P., Bäck, J., Keronen, P., Junninen, H., Petäjä, T., Kerminen, V.-M., and Kulmala, M.: Observations of ozone depletion events in a Finnish boreal forest, Atmos. Chem. Phys., 18, 49–63, https://doi.org /10.5194/acp-18-49-2018, 2018 .

Copernicus Climate Change Service (C3S) (2017): ERA5: Fifth generation of ECMWF atmospheric reanalyses of the global climate. Copernicus Climate Change Service Climate Data Store (CDS), date of access: 27.11.2024. https://cds.climate.copernicus.eu/cdsapp#!/home

De Marco, A., Anav, A., Sicard, P., Feng, Z., and Paoletti, E.: High spatial resolution ozone risk-assessment for Asian forests. Environmental Research Letters, 15(10), 104095, https://doi.org /10.1088/1748-9326/abb501, 2020.

Ducker, J. A., Holmes, C. D., Keenan, T. F., Fares, S., Goldstein, A. H., Mammarella, I., Munger, J. W. and Schnell, J.: Synthetic ozone deposition and stomatal uptake at flux tower sites. Biogeosciences, *15*(17), 5395-5413, https://doi.org /10.5194/bg-15-5395-2018, 2018.

Emberson, L.: Effects of ozone on agriculture, forests and grasslands. *Philosophical Transactions of the Royal Society A*, *378*(2183), 20190327, https://doi.org /10.1098/rsta.2019.0327, 2020.

Emmerichs, T.; Kerkweg, A.; Ouwersloot, H.; Fares, S.; Mammarella, I.; Taraborrelli, D.: A Revised Dry Deposition Scheme for Land–Atmosphere Exchange of Trace Gases in ECHAM/MESSy v2.54. Geoscientific Model Development, *14* (1), 495–519. https://doi.org /10.5194/gmd-14-495-2021, 2021.

Fares, S., Mereu, S., Scarascia Mugnozza, G., Vitale, M., Manes, F., Frattoni, M., ... and Loreto, F.: The ACCENT-VOCBAS field campaign on biosphere-atmosphere interactions in a Mediterranean ecosystem of Castelporziano (Rome):

93
94
95

site characteristics, climatic and meteorological conditions, and eco-physiology of vegetation. Biogeosciences, 6(6), 1043-1058, https://doi.org /10.5194/bg-6-1043-2009, 2009.

Fares, S. Measured and modelled stomatal and non-stomatal ozone fluxes in a mixed Mediterranean forest. In 25th ICP-Vegetation Task Force Meeting. gennaio–2 febbraio 2012, Brescia, Italia.,2012.

Fares, S., Savi, F., Muller, J., Matteucci, G., and Paoletti, E.: Simultaneous measurements of above and below canopy ozone fluxes help partitioning ozone deposition between its various sinks in a Mediterranean Oak Forest. Agricultural and Forest Meteorology, 198, 181-191. https://doi.org /10.1016/j.agrformet.2014.08.014, 2014.

Fares, S., Matteucci, G., Mugnozza, G. S., Morani, A., Calfapietra, C., Salvatori, E., ... and Loreto, F. : Testing of models of stomatal ozone fluxes with field measurements in a mixed Mediterranean forest. Atmospheric environment, 67, 242-251, https://doi.org /10.1016/j.atmosenv.2012.11.007, 2013.

Feng, Z., Tang, H., Uddling, J., Pleijel, H., Kobayashi, K., Zhu, J., ... and Guo, W.: A stomatal ozone flux–response relationship to assess ozone-induced yield loss of winter wheat in subtropical China. Environmental pollution, 164, 16-23. https://doi.org /10.1016/j.envpol.2012.01.014, 2012.

Fowler, D., Flechard, C., Cape, J.N. et al.: Measurements of Ozone Deposition to Vegetation Quantifying the Flux, the Stomatal and Non-Stomatal Components. Water, Air, & Soil Pollution 130, 63–74. https://doi.org /10.1023/A:1012243317471, 2001.

Fuhrer, J., Val Martin, M., Mills, G., Heald, C. L., Harmens, H., Hayes, F., ... and Ashmore, M. R.: Current and future ozone risks to global terrestrial biodiversity and ecosystem processes. Ecology and evolution, 6(24), 8785-8799. https://doi.org /10.1002/ece3.2568, 2016.

Ganzeveld, L., & Lelieveld, J.: Dry deposition parameterization in a chemistry general circulation model and its influence on the distribution of reactive trace gases. Journal of Geophysical Research: Atmospheres, 100(D10), 20999-21012. https://doi.org /10.1029/95JD02266, 1995.

833 Gerosa, G., Vitale, M., Finco, A., Manes, F., Denti, A. B. and Cieslik, S.: Ozone uptake by an evergreen Mediterranean

834 Forest (Quercus ilex) in Italy. Part I: Micrometeorological flux measurements and flux partitioning. Atmospheric

835 Environment, 39(18), 3255-3266, https://doi.org /10.1016/j.atmosenv.2005.01.056, 2005.

836

837 Gerosa, G., Marzuoli, R., Monteleone, B., Chiesa, M., and Finco, A.: Vertical ozone gradients above forests. Comparison of

838 different calculation options with direct ozone measurements above a mature forest and consequences for ozone risk

839 assessment. Forests, 8(9), 337. https://doi.org /10.3390/f8090337, 2017.

840 Gerosa G., Marzuoli R., Finco A.: Interannual variability of ozone fluxes in a broadleaf deciduous forest in Italy.

841 ELEMENTA: Science of the Anthropocene 10(1), 00105.  https://doi.org /10.1525/elementa.2021.00105, 2022.

842 Guaita P.R., Marzuoli R., Gerosa G.A.: A regional scale flux-based O3 risk assessment for winter wheat in northern Italy,

843 and effects of different spatio-temporal resolutions. Environmental Pollution 333, 121860, https://doi.org

844 10.1016/j.envpol.2023.121860, 2023.

845 Hardacre, C., Wild, O., and Emberson, L.: An evaluation of ozone dry deposition in global scale chemistry climate models,

846 Atmos. Chem. Phys., 15, 6419–6436, https://doi.org /10.5194/acp-15-6419-2015, 2015.

847 Hayes, F., Mills, G., Alonso, R., González-Fernández, I., Coyle, M., Grünhage, L., ... and Marzuoli, R.: A site-specific

848 analysis of the implications of a changing ozone profile and climate for stomatal ozone fluxes in Europe. Water, Air, & Soil

849 Pollution, 230, 1-15, https://doi.org /10.1007/s11270-018-4057-x, 2019.

850 Henne, S., Junkermann, W., Kariuki, J. M., Aseyo, J. and Klausen, J.: Mount Kenya Global Atmosphere Watch Station

851 (MKN): Installation and Meteorological Characterization. J. Appl. Meteor. Climatol., 47, 2946–2962,

852 https://doi.org /10.1175/2008JAMC1834.1, 2008a.

853 Henne, S., Klausen, J., Junkermann, W., Kariuki, J. M., Aseyo, J. O., and Buchmann, B.: Representativeness and

854 climatology of carbon monoxide and ozone at the global GAW station Mt. Kenya in equatorial Africa, Atmos. Chem. Phys.,

855 8, 3119–3139, https://doi.org /10.5194/acp-8-3119-2008, 2008b.

856 Hersbach, H., Bell, B., Berrisford, P., Hirahara, S., Horányi, A., Muñoz-Sabater, J., ... and Thépaut, J. N.: The ERA5 global

857 reanalysis. Quarterly Journal of the Royal Meteorological Society, 146(730), 1999-2049, https://doi.org /10.1002/qj.3803,

858 2020.

859 Horváth, L., Koncz, P., Móring, A. et al.: An Attempt to Partition Stomatal and Non-stomatal Ozone Deposition Parts on a
860 Short Grassland. Boundary-Layer Meteorol 167, 303–326, https://doi.org/10.1007/s10546-017-0310-x, 2018.

861 Huang, M., Crawford, J. H., Carmichael, G. R., Bowman, K. W., Kumar, S. V., and Sweeney, C.: Satellite soil moisture data
862 assimilation impacts on modeling weather variables and ozone in the southeastern US – Part 2: Sensitivity to dry-deposition
863 parameterizations, Atmos. Chem. Phys., 22, 7461–7487, https://doi.org /10.5194/acp-22-7461-2022, 2022.
864
865 Jägermeyr, J, Müller, C., Minoli, S., Ray, D., and Siebert., S.: GGCMI Phase 3 crop calendar [Data set]. Zenodo.
866 https://doi.org /10.5281/zenodo.5062513, 2021a.
867
868 Jägermeyr et al.: Climate impacts on global agriculture emerge earlier in new generation of climate and crop, Nature Food,
869 2, 873–885, https://www.nature.com/articles/s43016-021-00400-y, 2021b.
870
871 Junninen, H., Lauri, A., Keronen, P., Aalto, P., Hiltunen, V., Hari, P., Kulmala, M. 2009. Smart-SMEAR: online data
872 exploration and visualization tool for SMEAR stations. Boreal Environment Research 14, 447–457,
873 http://www.borenv.net/BER/pdfs/ber14/ber14-447.pdf, 2009.
874
875 Grulke, N. E. and Heath, R. L.: Ozone effects on plants in natural ecosystems. Plant Biology, 22, 12-37.
876 https://doi.org/10.1111/plb.12971, 2020.
877
878 Khan, A. M., Clifton, O. E., Bash, J. O., Bland, S., Booth, N., Cheung, P., ... and Stoy, P. C.: Ozone dry deposition through
879 plant stomata: Multi-model comparison with flux observations and the role of water stress as part of AQMEII4 Activity 2.
880 EGUsphere, 2024, 1-34. https://doi.org /10.5194/egusphere-2024-3038 , 2024.
881
882 Kattge, J. and Knorr, W.: Temperature acclimation in a biochemical model of photosynthesis: a reanalysis of data from 36
883 species. Plant, cell & environment, 30(9), 1176-1190, https://doi.org /10.1111/j.1365-3040.2007.01690.x, 2007.
884
885 Krause, D., & Thörnig, P.: JURECA: modular supercomputer at Jülich supercomputing centre. Journal of large-scale
886 research facilities JLSRF, *4*, A132-A132, https://doi.org /10.17815/jlsrf-4-121-1, 2018.
887
888 Li, M., Wu, P., & Ma, Z.: A comprehensive evaluation of soil moisture and soil temperature from third-generation
889 atmospheric and land reanalysis data sets. Int. J. Climatol, 40(13), 5744-5766, https://doi.org /10.1002/joc.6549, 2020.
890

891  Leung, F., Williams, K., Sitch, S., Tai, A. P., Wiltshire, A., Gornall, J., ... and Scoby, D.: Calibrating soybean parameters in
892  JULES 5.0 from the US-Ne2/3 FLUXNET sites and the SoyFACE-O$_3$ experiment. Geoscientific Model
893  Development, 13(12), 6201-6213, doi: 10.5194/gmd-13-6201-2020, 2020.
894
895  Mäkelä, J., Knauer, J., Aurela, M., Black, A., Heimann, M., Kobayashi, H., ... and Aalto, T.: Parameter calibration and
896  stomatal conductance formulation comparison for boreal forests with adaptive population importance sampler in the land
897  surface model JSBACH. Geoscientific Model Development, 12(9), 4075-4098. https://doi.org/10.5194/gmd-12-4075-2019,
898  2019.
899
900  McGrath, J. M., Betzelberger, A. M., Wang, S., Shook, E., Zhu, X. G., Long, S. P., & Ainsworth, E. A.: An analysis of
901  ozone damage to historical maize and soybean yields in the United States. Proceedings of the National Academy of Sciences,
902  *112*(46), 14390-14395, https://doi.org /10.1073/pnas.1509777112, 2015.
903
904  Meszaros, R., Horváth, L., Weidinger, T., Neftel, A., Nemitz, E., Dämmgen, U., ... and Loubet, B.: Measurement and
905  modelling ozone fluxes over a cut and fertilized grassland. Biogeosciences, 6(10), 1987-1999.
906  https://doi.org/10.5194/bg-6-1987-2009, 2009.
907
908  Meyers, T. P., Finkelstein, P., Clarke, J., Ellestad, T. G., and Sims, P. F.: A multilayer model for inferring dry deposition
909  using standard meteorological measurements. Journal of Geophysical Research: Atmospheres, 103(D17), 22645-22661,
910  https://doi.org/10.1029/98JD01564, 1998.
911
912  Mills, G., Hayes, F., Simpson, D., Emberson, L., Norris, D., Harmens, H. and Büker, P., Evidence of widespread effects of
913  ozone on crops and (semi-)natural vegetation in Europe (1990–2006) in relation to AOT40- and flux-based risk maps. Global
914  Change Biology, 17: 592-613, https://doi.org/10.1111/j.1365-2486.2010.02217.x, 2011.
915
916  Mills, G., Pleijel, H., Malley, C. S., Sinha, B., Cooper, O. R., Schultz, M. G., Neufeld, H. S., Simpson, D., Sharps, K., Feng,
917  Z., Gerosa, G., Harmens, H., Kobayashi, K., Saxena, P., Paoletti, E., Sinha, V., Xu, X.: Tropospheric Ozone Assessment
918  Report: Present-day tropospheric ozone distribution and trends relevant to vegetation. Elementa: Science of the
919  Anthropocene; 6 47, https://doi.org/10.1525/elementa.302, 2018.
920
921  Monks, P. S., Archibald, A. T., Colette, A., Cooper, O., Coyle, M., Derwent, R., ... and Williams, M. L.: Tropospheric ozone
922  and its precursors from the urban to the global scale from air quality to short-lived climate forcer. Atmospheric chemistry
923  and physics, *15*(15), 8889-8973. https://doi.org/10.5194/acp-15-8889-2015, 2015.

924

925 Pastorello, G., Trotta, C., Canfora, E.: The FLUXNET2015 dataset and the ONEFlux processing pipeline for eddy

926 covariance data. Sci Data 7, 225, https://doi.org/10.1038/s41597-020-0534-3, 2020.

927

928 Pieber, S.M., Henne, S., Nguyen, N.A., Nguyen, DL., Steinbacher, M.: Trace Gases and Air Quality in Northwestern

929 Vietnam During Recurrent Biomass Burning on the Indochina Peninsula Since 2014—Field Observations and Atmospheric

930 Simulations. In: Vadrevu, K.P., Ohara, T., Justice, C. (eds) Vegetation Fires and Pollution in Asia. Springer, Cham.

931 https://doi.org/10.1007/978-3-031-29916-2_32, 2023.

932

933 Pleim, J. and Ran, L.: Surface flux modeling for air quality applications. Atmosphere, 2(3), pp.271-302.

934 https://doi.org/10.3390/atmos2030271, 2011.

935

936 Poyatos, R., Granda, V., Flo, V., Adams, M. A., Adorján, B., Aguadé, D., ... and Van Der Tol, C.: Global transpiration data

937 from sap flow measurements: the SAPFLUXNET database. Earth System Science Data, 13, 2607–2649,

938 https://doi.org/10.5194/essd-13-2607-2021, 2021.

939

940 Putaud J.P., Bergamaschi, P., Bressi, M., Cavalli, F., Cescatti, A., Daou, D., Dell'Acqua, A., Douglas, K., Duerr, M.,

941 Fumagalli, I., Goded, I., Grassi, F., Gruening, C., Hjorth, J., Jensen, N. R., Lagler, F., Manca, G., Martins Dos Santos, S.,

942 Matteucci, M., , Passarella, R., Pedroni, V., Pokorska, O., Roux, D.: JRC – Ispra Atmosphere - Biosphere - Climate

943 Integrated monitoring Station: 2014 Report; EUR 27639 EN, https://doi.org/10.2788/570407, 2014.

944

945 Ran, L., Pleim, J., Song, C., Band, L., Walker, J.T. and Binkowski, F.S.: A photosynthesis-based two-leaf canopy stomatal

946 conductance model for meteorology and air quality modeling with WRF/CMAQ PX LSM. Journal of Geophysical Research:

947 Atmospheres, 122(3), pp.1930-1952, https://doi.org/10.1002/2016JD025583, 2017.

948

949 Raghav, P., Kumar, M., and Liu, Y.: Structural constraints in current stomatal conductance models preclude accurate

950 estimation of evapotranspiration and its partitions, https://doi.org/10.1029/2024WR037652, 2023.

951

952 Ramya, A., Dhevagi, P., Poornima, R., Avudainayagam, S., Watanabe, M., and Agathokleous, E.: Effect of ozone stress on

953 crop productivity: A threat to food security. *Environmental Research*, 116816. https://doi.org/10.1016/j.envres.2023.116816,

954 2023.

955

956 Savi, F. and Fares, S.: Ozone dynamics in a Mediterranean Holm oak forest: comparison among transition periods

957 characterized by different amounts of precipitation. Annals of Silvicultural Research 38(1) 1-6

958 http://dx.doi.org/10.12899/ASR-801, 2014

959

960 Schröder, S., Schultz, M. G., Selke, N., Sun, J., Ahring, J., Mozaffari, A., Romberg, M., Epp, E., Lensing, M., Apweiler, S.,

961 Leufen, L. H., Betancourt, C., Hagemeier, B., Rajveer, S.: TOAR Data Infrastructure,

962 https://doi.org/10.34730/4d9a287dec0b42f1aa6d244de8f19eb3, 2021.

963

964 Schucht, S., Tognet, F., Létinois, L. and Ineris, I.N.: Wheat yield loss in 2019 in Europe due to ozone exposure, Eionet

965 Report-ETC/ATNI, 2021.

966

967 Silva, S. J. and Heald, C. L.: Investigating dry deposition of ozone to vegetation. Journal of Geophysical Research:

968 Atmospheres, 123(1), 559-573. https://doi.org/10.1002/2017JD027278, 2018.

969

970 Stella, Patrick, et al.: Predicting and partitioning ozone fluxes to maize crops from sowing to harvest: the Surfatm-O 3

971 model, Biogeosciences 8.10, 2869-2886. https://doi.org/10.5194/bg-8-2869-2011, 2011.

972

973 Stella, P., Personne, E., Lamaud, E., Loubet, B., Trebs, I., & Cellier, P. (2013). Assessment of the total, stomatal, cuticular,

974 and soil 2 year ozone budgets of an agricultural field with winter wheat and maize crops, Journal of Geophysical Research:

975 Biogeosciences, 118(3), 1120-1132, https://doi.org/10.1002/jgrg.20094, 2013.

976

977 Sofen, E. D., Bowdalo, D., Evans, M. J., Apadula, F., Bonasoni, P., Cupeiro, M., ... and Tørseth, K.: Gridded global surface

978 ozone metrics for atmospheric chemistry model evaluation. Earth System Science Data, 8(1), 41-59,

979 https://doi.org/10.5194/essd-8-41-2016, 2016.

980

981 Sun, S., Tai, A. P. K., Yung, D. H. Y., Wong, A. Y. H., Ducker, J. A., and Holmes, C. D.: Influence of plant ecophysiology

982 on ozone dry deposition: comparing between multiplicative and photosynthesis-based dry deposition schemes and their

983 responses to rising $CO_2$ level, Biogeosciences, 19, 1753–1776, https://doi.org/10.5194/bg-19-1753-2022, 2022.

984

985 Tai, A. P., Yung, D. H., & Lam, T. : Terrestrial Ecosystem Model in R (TEMIR) version 1.0: simulating ecophysiological

986 responses of vegetation to atmospheric chemical and meteorological changes. Geoscientific Model Development, 17(9),

987 3733-3764, https://doi.org/10.5194/gmd-17-3733-2024, 2024.

988

989    Travis, K. R. and Jacob, D. J.: Systematic bias in evaluating chemical transport models with maximum daily 8 h average

990    (MDA8) surface ozone for air quality applications: a case study with GEOS-Chem v9. 02. Geoscientific Model

991    Development, 12(8), 3641-3648. https://doi.org/10.5194/gmd-12-3641-2019, 2019.

992

993    UNECE LRTAP (2017). III. Mapping critical levels for vegetation. Available at:

994    https://icpvegetation.ceh.ac.uk/sites/default/files/FinalnewChapter3v4Oct2017_000.pdf

995    Visser, A. J., Ganzeveld, L. N., Goded, I., Krol, M. C., Mammarella, I., Manca, G., and Boersma, K. F.: Ozone deposition

996    impact assessments for forest canopies require accurate ozone flux partitioning on diurnal timescales, Atmos. Chem. Phys.,

997    21, 18393–18411, https://doi.org/10.5194/acp-21-18393-2021, 2021.

998

999    Walker, A. P., Quaife, T., Van Bodegom, P. M., De Kauwe, M. G., Keenan, T. F., Joiner, J., ... & Woodward, F. I.: The

1000    impact of alternative trait-scaling hypotheses for the maximum photosynthetic carboxylation rate ($V_{Cmax}$) on global gross

1001    primary production. *New Phytologist*, *215*(4), 1370-1386, https://doi.org/10.1111/nph.14623, 2017:

1002

1003    Wang, T., Wang, F., Song, H., Zhou, S., Ru, X. and Zhang, H.: Maize yield reduction and economic losses caused by

1004    ground-level ozone pollution with exposure-and flux-response relationships in the North China Plain. Journal of

1005    Environmental Management, 324, p.116379. https://doi.org/10.1016/j.jenvman.2022.116379, 2022.

1006

1007    Wilkinson, M. D., Dumontier, M., Aalbersberg, I. J., Appleton, G., Axton, M., Baak, A., ... & Mons, B.: The FAIR Guiding

1008    Principles for scientific data management and stewardship. Scientific data, 3(1), 1-9.

1009    https://doi.org/10.1038/sdata.2016.18, 2016.

1010

1011    Wong, A. Y. H., Geddes, J. A., Ducker, J. A., Holmes, C. D., Fares, S., Goldstein, A. H., et al.: New evidence for the

1012    importance of non-stomatal pathways in ozone deposition during extreme heat and dry anomalies. Geophysical

1013    ResearchLetters, 49, e2021GL095717, https://doi.org/10.1029/2021GL095717, 2022.

1014

1015    Yen M-Ch. , Peng C-M., Chen T.-C., Chen Ch.-S., Lin N.-H., Tzeng R.-Y., Lee Y.-A. , Lin Ch.-Ch.: Climate and weather

1016    characteristics in association with the active fires in northern Southeast Asia and spring air pollution in Taiwan during 2010

1017    7-SEAS/Dongsha Experiment, Atmospheric Environment, Volume 78, Pages 35-50,

1018    https://doi.org/10.1016/j.atmosenv.2012.11.015, 2013.

1019

1020 Young, P. J.; Naik, V.; Fiore, A. M.; Gaudel, A.; Guo, J.; Lin, M.; Neu, J.; Parrish, D.; Rieder, H.;Schnell, J. others.:

1021 Tropospheric Ozone Assessment Report: Assessment of Global-Scale Model Performance for Global and Regional Ozone

1022 Distributions, Variability, and Trends. Elem Sci Anth, 6 (1), https://doi.org/10.1525/elementa.265, 2018.

1023

1024 Zhang, L., Brook, J. R., and Vet, R.: A revised parameterization for gaseous dry deposition in air-quality models, Atmos.

1025 Chem. Phys., 3, 2067–2082, https://doi.org/10.5194/acp-3-2067-2003, 2003.

1026

1027 Zhang, W., Feng, Z., Wang, X., Liu, X., & Hu, E.: Quantification of ozone exposure-and stomatal uptake-yield response

1028 relationships for soybean in Northeast China. Science of the Total Environment, 599, 710-720,

1029 https://doi.org/10.1016/j.scitotenv.2017.04.231, 2017.

1030

1031
1032
1033
1034
1035
1036
1037
1038
1039

1040

1041

1042

1043

1044

1045

1046 **Appendix**

1047 Table A1: Abbreviations

| Symbol | Long name |
|---|---|
| rsmin | Minimum stomatal resistance in [s m$^{-1}$] |
| gsmax | Maximum stomatal conductance in [m s$^{-1}$] |
| RH | Relative humidity in [%] |
| LAI | Leaf area index in [m$^2$ m$^{-2}$] |
| sd, sn | snow depth in [m] and snow cover |
| ssrd, strd | solar and thermal flux at surface in [W m$^{-2}$] |
| sw | Soil wetness [m] |
| al_vis: | albedo (visible) |
| cwv | canopy water content in [kg m$^{-2}$] |
| SWC | Soil water content |
| SM | Soil moisture [m$^3$m$^{-3}$] |
| wdir | geo wind direction [°] |
| wspeed | Wind speed in [m s$^{-1}$] |
| cv | Vegetation fraction [m$^2$m$^{-2}$] |
| P | Precipitation in [mm] |
| P_rate | Precipitation rate in [mm h$^{-1}$], [kg m$^{-2}$ s$^{-1}$], [m s$^{-1}$] |
| Tair, Tsoil, T2m | Air, soil, 2m temperature in [K] |
| VPD | Vapour pressure deficit [kPa] |
| Pa | Air pressure [hPa] |
| Rn, Gr | Net and global radiation [W m$^{-2}$] |
| u* | Friction velocity [m s$^{-1}$] |
| O$_3$, CO$_2$ | O$_3$ and CO$_2$ concentration in [ppb] und [ppt] |
| h_dis, z0 | Displacement height [m], roughness length [m] |
| CF | Cloud fraction |
| LUC | Land usage category |

1048

1049

123
124
125